Contributions to Mineralogy and Petrology (2020) 175:71
https://doi.org/10.1007/s00410-020-01709-w

ORIGINAL PAPER

# Eclogites of the North Atlantic Craton: insights from the Chidliak eclogite xenoliths (S. Baffin Island, Canada)

**Vedran Pobric**[1] · **Nester Korolev**[1,2] · **Maya Kopylova**[1]

Received: 9 December 2019 / Accepted: 19 June 2020 / Published online: 8 July 2020


## Abstract

The 156–138 Ma Chidliak kimberlites on the Eastern Hall peninsula (EHP) of Baffin Island entrained mantle xenoliths interpreted to have been a part of the Archean North Atlantic Craton (NAC) lithospheric mantle. We studied 19 Chidliak eclogite xenoliths that comprise 10 bimineralic, 5 rutile-bearing, 3 orthopyroxene-bearing and 1 kyanite-bearing eclogites. We report major and trace element compositions of the minerals, calculated bulk compositions, pressures and temperatures of the rock formation and model melt extraction from viable protoliths. The eclogite samples are classified into three groups of HREE-enriched, LREE-depleted and metasomatized based on their reconstructed whole-rock REE patterns. PT parameters of the eclogites were calculated by projecting garnet–clinopyroxene temperatures onto the local *P–T* arrays for 65 Chidliak peridotite xenoliths. All Chidliak eclogites are equilibrated in the diamond *P–T* field and cluster in two groups, low-temperature ($n = 5$, 840–990 °C at 4.1–5.0 GPa) and high-temperature ($n = 11$, $T > 1320$ °C at $P > 7.0$ GPa). The reconstructed Mg-rich major element bulk compositions and trace elements patterns are similar to Archean basalts from the North Atlantic and Superior cratons and the oceanic gabbros. The LREE-depleted Chidliak eclogites could be residues after 15–55% partial melting of Archean basalt at the eclogite facies of metamorphism that led to extraction of a tonalite–trondhjemite–granodiorite melt from the EHP. The HREE-depleted eclogites may have experienced a lower degree (<10%) of partial melting. Two eclogites may have formed after the gabbro protolith based on the presence of kyanite, high Sr content of garnet and positive Eu anomalies in garnet and bulk eclogite compositions. The metasomatism is reflected in higher Ce/Yb, Sr/Y, $TiO_2$ or MgO of the eclogites. The average contents of MgO, FeO and CaO in NAC eclogites are statistically distinct from those in Slave craton eclogites with a probability of >95%. The former are more magnesian, less ferrous and calcic, contain more magnesian and less calcic garnets, and lower proportions of group C eclogites. The contrast may relate to the stronger NAC metasomatism by silicate–carbonate melt observed in Chidliak peridotitic mantle, or to the different formation ages of the eclogites beneath the two cratons.

**Keywords** Chidliak · Kimberlite · Eclogite · Metasomatism · Xenoliths · North Atlantic Craton

## Introduction

The mantle of the North Atlantic Craton (NAC) is relatively poorly studied compared to the well-documented mantle of such cratons as Kaapvaal or Slave. The NAC has been rifted into several fragments, the largest of which is in southern Greenland, and the others are in the Nain Province

Communicated by Timothy L Grove.

**Electronic supplementary material** The online version of this article (https://doi.org/10.1007/s00410-020-01709-w) contains supplementary material, which is available to authorized users.

✉ Nester Korolev
nkorolev@eoas.ubc.ca

Vedran Pobric
vpobric@eoas.ubc.ca

Maya Kopylova
mkopylov@eos.ubc.ca

[1] Department of Earth, Ocean and Atmospheric Sciences, University of British Columbia, 2020-2207 Main Mall, Vancouver, BC V6T 1Z4, Canada

[2] Institute of Earth Sciences, Saint-Petersburg State University, 199034, Universitetskaya nab., 7-9, St. Petersburg, Russia

(Canada) (Fig. 1) and in the Lewisian complex of NW Scotland (Pearson and Wittig 2014). Recent study of peridotite xenoliths from the Chidliak kimberlite province on the Baffin Island (NE Canada) indicated that the Chidliak mantle in the Archean was likely contiguous with the NAC mantle (Kopylova et al. 2019), confirming conclusions from the crustal geology (Scott et al. 2002; St-Onge et al. 2002). NAC assembly is widely considered a prime example of

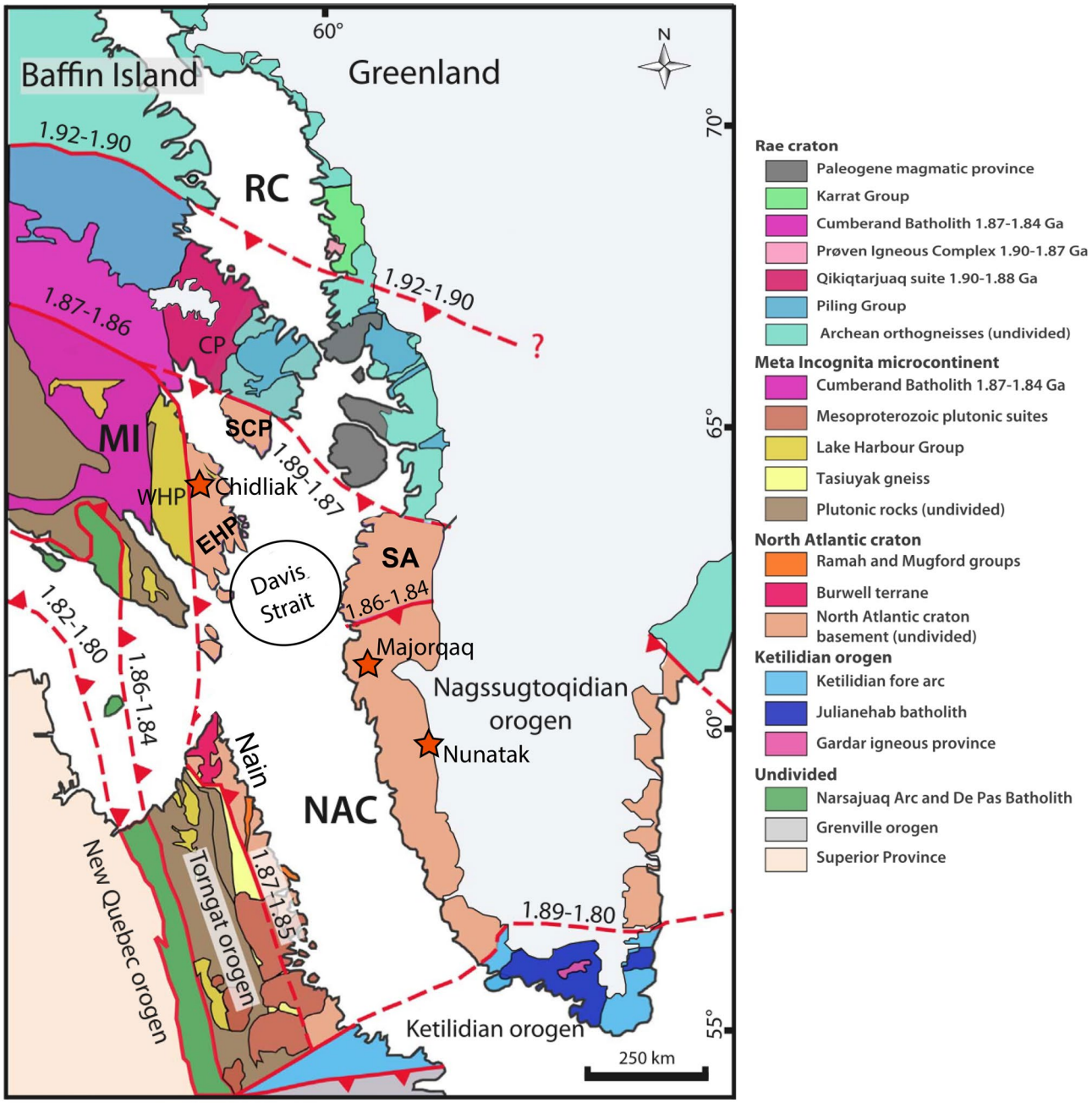


**Fig. 1** The inferred extent of the NAC based on the regional crustal correlation model of From et al. (2018) and the mantle correlation of Kopylova et al. (2019). The map is based on the 120 Ma reconstruction model of North America–Greenland margins. The red boundaries are interpreted crustal sutures with dates indicating the timing of terrane accretion in Ga (From et al. 2018). *EHP* eastern Hall Peninsula, *WHP* western Hall Peninsula, *NAC* North Atlantic Craton, *SCP* Southern Cumberland Peninsula, *Nain* Nain block of NAC, *SA* Southern Aasiaat domain, *MI* Meta Incognita microcontinent, *RC* Rae Craton, *CP* Cumberland Peninsula. Circle labeled "Davis Strait" is localization of the preserved continental lithosphere between the Labrador Sea and the Baffin Bay (Heron et al. 2019). Red stars are study areas for the Chidliak (this work) and Nunatak-1390 (Tappe et al. 2011) eclogite xenoliths and Archean metapelitic eclogites of the Majorqaq belt (Dyck et al. 2015). The color geological legend is modified after From et al. (2018)

craton formation by subduction and collision processes (Windley and Garde 2009; Dyck et al. 2015). Mantle eclogites, which are commonly interpreted as samples of metamorphosed subducted crust entrained by deep volatile-rich NAC magmas could provide an invaluable insight into the craton formation. So far, two suites of NAC eclogites are described, one from the cratonic mantle (Tappe et al. 2011), and one from the lower crust (Sajeev et al. 2013). This work reports on a third, previously unknown suite of NAC eclogite xenoliths from a different geographic locality on SE Baffin Island, more than doubling the amount of studied NAC mantle eclogite samples.

The 156–138 Ma (Heaman et al. 2015) Chidliak kimberlite was emplaced in the eastern part of the hall peninsula block (EHP, Fig. 1) composed of Archean gneiss with tonalite–monzogranite–syenogranite composition with local ultramafic pods (From et al. 2018 and references therein) and is overlain by ca. 300 m of Lower Paleozoic limestones (Pell et al. 2013). The tonalite and monzogranite crystallized at 2976 ± 4 (U–Pb ages on zircon, From et al. 2018) to 2720 ± 4 Ma and experienced subsequent metamorphism at ca. 2740–2700 Ma. EHP lithospheric mantle is overlain by a 40 km thick crust (Fig. 5 of Thompson et al. 2010). The HP Block lithosphere–asthenosphere boundary as determined by surface wave inversions (SdP CCP) and confirmed by shear velocity analysis is at ~210 km (Fig. 6 of Porritt et al. 2015), which is close to the 220–250 km deep petrological lithosphere (Kopylova et al. 2019).

The studied xenoliths were collected by Peregrine Diamonds Ltd. from surface outcrops, trenching and drill-core, selected for their size and macroscopic freshness. Petrography, major and trace element chemistry, and geothermobarometry for 19 eclogite xenoliths serve as a basis for conclusions on the nature of the crustal protoliths. We interpret the Chidliak eclogites, which are distinctly less calcic and ferrous than mantle eclogites of the neighboring Slave craton, as metamorphosed Archean basalts or gabbros. We also explore various petrological expressions of metasomatism in the eclogites trapped in the strongly metasomatized NAC peridotitic mantle for billions of years (Kopylova et al. 2019). Finally, we comment on the depth location of the eclogites, which may have locally protected the base of the NAC lithosphere from later rifting and oceanization.

## Tectonic history of the NAC

The NAC began to assemble from small TTG blocks formed in arc settings by partial melting of hydrous mafic crust recycled to amphibolite or eclogite facies conditions between 3.8 and 2.8 Ga (Tappe et al. 2011; Windley and Garde 2009). These proto-continents merged as a result of SE-dipping subduction and closure of back-arc basins (Dyck et al. 2015 and references therein; Windley and Garde 2009). Two Greenland NAC terranes, Faringehavn and Majorqaq, provide abundant and convincing evidence for a Neoarchean orogeny at 2.72–2.56 Ga, i.e., high-P metamorphism and a clockwise *P–T* path (Dyck et al. 2015 and references therein). The direction of the subduction that closed the oceanic basin between the northern-most block of Greenland NAC and the five southern amalgamated blocks was suggested as south-dipping to explain generation of coeval granites to the south (Dyck et al. 2015).

The better known NAC Proterozoic history involves many episodes of orogeny and accretion, all related to subduction of oceanic slabs. The most important episodes focus on the Trans Hudson Orogen and assembly of northeastern Laurentia 1.88–1.80 Ga. The orogenic events included: (1) accretion of the Meta-Incognita microcontinent to the Rae craton southern margin at 1.88 Ga; (2) accretion of the Aasiaat domain to the southern margin of the Rae craton of Greenland; (3) collision of the eastern margin of the Meta Incognita with the NAC at 1.87–1.85 Ga; (4) collision of the composite Rae craton with the composite NAC at 1.86–1.84 Ga; (5) accretion of the arc terranes and terminal collision of the composite domains with the Superior craton south at 1.82 and 1.80 Ga (From et al. 2018).

Petrological study of ~120 peridotite xenoliths from the Chidliak kimberlite province indicated that its mantle was likely contiguous with the NAC mantle before 1.8 Ga, based on the following evidence summarized in Kopylova et al. (2019): (1) similarities of mineral and wehrlite-rich bulk compositions of mantle xenoliths in SW Greenland and Chidliak; (2) strong contrast in olivine compositions, proportions of harzburgites and wehrlites with the adjacent mantle of the Northern Superior craton (Hunt et al. 2012); (3) archean Re-Os minimum ages ($T_{RD}$) preserved in two thirds of studied Chidliak peridotites (Liu et al. 2017); (3) Neoarchean and Paleoproterozoic Re-Os ages ($T_{RD}$ = 2.8 Ga and 2.0 Ga) ages of the original melt depletion for the Greenlandic NAC mantle (Pearson and Wittig 2014). The above data indicate that the EHP mantle that hosts the Chidliak kimberlite merged with the NAC and jointly experienced silicate–carbonate metasomatism (Kopylova et al. 2019) some time before the amalgamation of the NAC with the superior craton at ca. 1.8 Ga, as the metasomatism is not observed in the northern superior craton mantle.

The conclusions on the age and longevity of the joint Chidliak–NAC mantle are further supported by independent data on the crustal history of NE Canada and Greenland, which is based on larger and more detailed datasets. The large expanse of the NAC mantle with similar mineralogical and compositional features is not mirrored in the more complex crustal geology. The crust of the NAC is composed of the following blocks (Fig. 1): (1) eastern hall peninsula (EHP); (2) the meta incognita microcontinent which includes the Western HP; (3) Cumberland Peninsula; (4)

Southern Cumberland Peninsula; (5) Nain block of NAC (NE Labrador); (6) Greenland part of NAC; (7) Aasiaat domain (From et al. 2018) and (8) the Lewisian Complex (Scotland; Pearson and Wittig 2014). Each of these blocks differ in their magmatic and metamorphic histories, and the most recent detailed studies of the U–Pb zircon age correlations enabled conclusions on the degrees of similarities between the blocks' geology. The studies unified EHP, southern Cumberland peninsula and the southern Aasiaat domain in a single Archean block with a shared geological history since at least ca. 2.75–2.69 Ga, and clearly separated the block from the western HP (From et al. 2018). The EHP and NAC of Northern Labrador and Greenland were likely not juxtaposed prior to Archean tectonic amalgamation at ca. 2.75–2.69 Ga (From et al. 2018). The EHP–Southern Cumberland–Aasiaat domain block is much closer based on the geological history to the NAC of SW Greenland and Labrador, than to the Meta Incognita microcontinent (Fig. 7 of From et al. 2018). The above crustal and mantle correlations suggest that the large crustal block of EHP + Southern Aasiat domain + Southern Cumberland Peninsula was contiguous with the NAC on the south until the opening of the Labrador Sea heated and decratonized exclusively the Aasiaat domain mantle (Kopylova et al. 2019) developing the Paleogene Magmatic Province (From et al. 2018). The data for the gabbro (212 whole-rock samples) and MORB (4097 whole-rock samples and 17 737 samples of glasses) fields were downloaded from the PetDB Database (www.earthchem.org/petdb) and taken from single references (Online Resource 5). The gabbro field is based on the modern oceanic and ancient ophiolite gabbro dataset. The MORB field is based on compositions of whole-rock and NMORB glasses (normal MORB), EMORB (enriched MORB), DMORB (depleted MORB) and back-arc spreading center basalts (Online Resource 5). The data for the Superior Archean basalt (SAB) (98 whole-rock samples), NAC Archean basalt (NACB) (171 whole-rock samples) and komatiite (1825 whole-rock samples) fields were downloaded from the GEOROC Database (https://georoc.mpch-mainz.gwdg.de) (Online Resource 5). The SAB field comprises komatiitic basalts and picrites of Archean age from the Superior craton. The NACB field represents non-komatiitic basalts and picrites of Archean age from the NAC. The komatiite field includes only komatiite compositions of Archean age (Kerr and Arndt 2001)

### Eclogites of the NAC

Prior to this study, eclogites were unknown from the EHP, but were reported from other rifted blocks of the NAC. Eclogite xenoliths were found in the Jurassic Nunatak-1390 kimberlite of West Greenland (Fig. 1, Tappe et al. 2011). The xenoliths were interpreted as refractory residues of TTG melt extraction from an oceanic basaltic slab in an Archean subduction zone, which is shown by (1) an excellent compositional match between NAC TTG gneisses of the Tasiusarsuaq terrane and Nunatak-1390 eclogites with experimental products for shallow partial melting of metabasalt; (2) complementarity of NAC TTG, Nunatak-1390 eclogites and pillow basalts from the Late Archean Ivisaartoq greenstone belt in the central NAC; (3) a broad age overlap between the 2.9–2.7 Ga NAC TTGs and the 2.70 ± 0.29 Ga Nunatak-1390 eclogites (a Pb–Pb secondary isochron, Tappe et al. 2011).

The far eastern corner of the NAC, the Lewisian Gneiss Complex of NW Scotland, went through peak eclogite-facies metamorphism at 2.4–2.2 GPa and 1060–1040 °C between ca. 2480 and 2330 Ma (Sajeev et al. 2013). These lower crustal eclogites equilibrated at a high metamorphic field gradient incompatible with the cold cratonic mantle geotherm of the Nunatak-1390 eclogites. The authors proposed that the Lewisian crust was comprised of layered mafic–ultramafic complexes formed in an oceanic environment. The retrogressed Lewisian eclogites have the highest pressures so far reported for Archean crustal rocks and, in the opinion of Sajeev et al. (2013), "necessitate subduction" to provide the imperative PT conditions and fluid activity for the prerequisite high-pressure mineralogy.

All NAC eclogites range in ages from 2.70 ± 0.29 Ga (Tappe et al. 2011) to 2.48–2.33 Ma (Sajeev et al. 2013) despite the rich 1.8 Ga orogenic history of EHP and its bounding by younger Paleoproterozoic orogens from all sides (Fig. 1).

## Methods and materials

Quantitative major element mineral analyses were undertaken on a CAMECA SX-50 electron microprobe at the University of British Columbia, Department of Earth, Ocean and Atmospheric Sciences (EOAS), Vancouver, Canada. At least 3 garnet and 3 clinopyroxene grains were probed per each thin section, and each grain was analyzed at their core and rim (Online Resource 1). All elements were analyzed with a beam current of 20 nA, an acceleration voltage of 15 kV, and peak count times of 20 s and 10 s on the background. Longer counts (40 s and 60 s on the peak and 20 s and 30 s on the background) were used for K in pyroxene and Na in garnet, respectively. The beam diameter was 5 µm for silicate minerals and 2 µm for rutile. Data reduction was made using the 'PAP' φ(ρZ) method (Pouchou and Pichoir 1985). See Online Resource 1 for the accuracy, minimum detection limits, crystals and standards of the analyses.

Trace elements were measured in primary minerals in the 15 less altered samples on grains analyzed for major elements. The analyses were done by laser ablation (LA)-inductively coupled plasma mass spectrometer (ICP-MS) at the Pacific Centre for Isotopic and Geochemical Research at the University of British Columbia. LA-ICP-MS analyses were carried out with an ArF excimer laser ablation system (193 nm; Resolution M-50LR, ASI Australia) connected to a Quadrupole ICP-MS (Agilent 7700x). Measurements were performed at a repetition rate of 8 Hz and using a beam diameter of 89 µm. Energy density on the sample was 1.8 J/cm$^2$. Helium served as a carrier gas and was admixed with $N_2$ for signal enhancement. The mass spectrometer was tuned for sensitivity, ThO/Th < 0.3% and a mass bias with 238/232 < 110%. Calibration was carried out using the silicate glass standard SRM NIST612 as external standard and Ca (43) as an internal standard using values from EPMA analyses. SRM NIST610 and the basaltic BCR2-G were cross-checked for quality control. Data reduction was performed by the Iolite v.3 software (Paton et al. 2011). The data, including the accuracy and minimum detection limits, are given in Online Resource 2.

## Results

### Petrography

Eclogites account for 10.6% of the mantle xenolith collection ($n = 165$) obtained from kimberlite pipes CH-07, CH-06, and CH-44. The eclogite xenoliths are round, texturally massive, 1–12 cm in size and include 10 bimineralic, 5 rutile-bearing (0.5–3 vol% of rutile), 3 orthopyroxene-bearing (9–11 vol%) and one kyanite-bearing (<20 vol%) assemblages (Table 1; Online Resource 3). Orthopyroxene-bearing samples were classified as eclogites rather than pyroxenites based on the proportion of rock-forming minerals (15–66 vol% Cpx, 23–72% Grt and 9–11% Opx) and omphacitic composition of clinopyroxene, in accordance with the IUGS (International Union of Geological Sciences) Subcommission on the Systematics of Metamorphic Rocks recommendations (Cpx + Grt ≥ 75 vol%, Grt ≥ 5 and Cpx ≥ 5 vol%, Cpx is omphacite) (Desmons and Smulikowski 2007).

Chidliak eclogites show coarse-grained granoblastic texture with a typical grain size of 1–7 mm. Xenoblastic to hypidioblastic grains of garnet (23–72 vol%) and clinopyroxene (15–77 vol%) occur together with rounded xenoblastic orthopyroxene and rutile (0.1–1 mm) and elliptical to tear-shaped kyanite (1.5 mm on average). Dark brown rutile contains ilmenite exsolution lamellae. Mineral modes and sample photographs are presented in Online Resource 3.

Secondary minerals replace more than 30 vol% of eclogites, and clinopyroxene is the most significantly affected. In 14 out of 18 specimens, secondary clinopyroxene replaces ~25% of the primary mineral comprising "cloudy" areas in peripheral parts and adjacent to fractures. Past studies ascribed the origin of similar textures of secondary clinopyroxene to partial melting (e.g., Misra et al. 2004; Taylor and Neal 1989). In samples CH-S8 and CH-S9, clinopyroxene was completely replaced by a chlorite-rich fine intergrowth of secondary minerals. Orthopyroxene is extensively serpentinized, while kyanite is replaced on its margins by fibrous corundum. Secondary amphibole and euhedral small spinel form a kelyphitic assemblage that replaces garnet rims. Interstitial round sulfide grains are very abundant in some samples, attesting to a possible late origin of the sulfidization. Phlogopite was found both as laths and as an interstitial phase between clinopyroxenes and garnets. Thin veins of calcite, serpentine, zeolites cut the samples, and amphibole commonly occurs interstitially, replacing clinopyroxene and garnet.

### Classification based on the reconstructed whole-rock REE patterns

Reconstructed major and trace element bulk compositions are free from effects of secondary alteration and can potentially be used for genetic inferences (e.g., Aulbach and Jacob 2016; Jacob 2004) and classification. We reconstructed bulk rock compositions for the eclogites (Table 1; Online Resource 4) from analyzed garnet and clinopyroxene, orthopyroxene and rutile compositions (Table 2) and observed modal mineralogy. The mineral modes were assessed by point-counting technique with accuracy of 10 vol% for rock-forming phases based on photos of cut macrospecimens and thin sections (Online Resource 3).

The reconstructed whole-rock (RWR) REE patterns are relatively insensitive to garnet or clinopyroxene modes (Aulbach et al. 2007) and, unlike major element whole-rock compositions, show three discrete groups we identify as (1) HREE-enriched, (2) LREE-depleted and (3) metasomatized. The HREE-enriched xenoliths show wavy patterns with low LREE in comparison to HREE ($La_N/Lu_N = 0.17–0.53$) (Fig. 2a). The LREE-depleted eclogites have patterns with strong depletions in LREE (La, Ce and Pr ≤ 0.1 NMORB level, $La_N/Lu_N = 0.04–0.24$) and flattened HREE (Fig. 2b). The three metasomatized eclogites show sub-horizontal REE patterns with LREE enrichment ($La_N/Lu_N = 1.28–3.12$) (Fig. 2c). The majority of eclogites have REE contents below the average NMORB level (0.02–0.9) (Gale et al. 2013); only two samples with HREE-enriched patterns show HREE concentrations up to three times higher than in the average NMORB (Fig. 2).

The metasomatized and HREE-enriched eclogites have a relatively narrow Mg# range of 71–89, while three out of five LREE-depleted eclogites have an Mg# range of 55–67.

**Table 1** Major and trace element reconstructed whole-rock compositions of the Chidliak eclogites

| Sample | Q-A | Q-B | CH-6 | CH-7 | CH-N1 | CH-S3 | CH-S4 | CH-D27-80 | CH-D28 | CH-D27-184 | CH-S8 | CH-S10 | CH-S13 |
|---|---|---|---|---|---|---|---|---|---|---|---|---|---|
| Min. a | Rt-Opx | Rt | Bimin | Bimin | Bimin | Bimin | Rt | Bimin | Rt-Opx | Rt | Bimin | Bimin | Bimin |
| Ecl. Type | Met | Met | H-en. | Met | L-dep. | H-en. | – | H-en. | L-dep. | L-dep. | – | L-dep. | H-en. |
| Cpx | 0.66 | 0.54 | 0.56 | 0.77 | 0.55 | 0.61 | 0.62 | 0.50 | 0.15 | 0.68 | 0.53 | 0.45 | 0.65 |
| Grt | 0.23 | 0.45 | 0.44 | 0.23 | 0.45 | 0.36 | 0.36 | 0.50 | 0.72 | 0.30 | 0.47 | 0.55 | 0.35 |
| Opx | 0.09 | – | – | – | – | – | – | – | 0.11 | – | – | – | – |
| Rt | 0.02 | 0.01 | – | – | – | 0.03 | 0.02 | – | 0.02 | 0.02 | – | 0.005 | 0.005 |
| Ky | – | – | – | – | – | – | – | – | – | – | – | – | – |
| A–B–C type | A | B | B | B | B | A | B | A | A | B | | B | B |
| $SiO_2$ (wt%) | 51.23 | 48.66 | 49.29 | 51.37 | 48.28 | 48.20 | 48.12 | 48.25 | 45.19 | 48.36 | – | 46.88 | 51.07 |
| $TiO_2$ | 2.25 | 1.53 | 0.41 | 0.55 | 0.57 | 0.23 | 2.13 | 0.23 | 0.35 | 2.37 | – | 0.78 | 0.43 |
| $Al_2O_3$ | 8.17 | 13.18 | 13.31 | 11.89 | 14.93 | 10.02 | 11.28 | 13.83 | 17.55 | 11.72 | – | 15.27 | 11.70 |
| $Cr_2O_3$ | 0.15 | < MDL | 0.04 | 0.36 | 0.33 | 0.15 | < MDL | 0.14 | 0.17 | < MDL | – | < MDL | 0.14 |
| FeO | 4.01 | 10.05 | 7.05 | 6.38 | 8.21 | 6.20 | 10.84 | 9.21 | 6.95 | 12.06 | – | 10.83 | 6.52 |
| MnO | 0.15 | 0.25 | 0.18 | 0.07 | 0.14 | 0.13 | 0.15 | 0.18 | 0.27 | 0.18 | – | 0.21 | 0.17 |
| MgO | 18.81 | 13.92 | 16.92 | 11.64 | 11.83 | 15.94 | 10.99 | 15.72 | 21.85 | 8.37 | – | 12.43 | 16.53 |
| CaO | 12.98 | 10.78 | 9.93 | 12.84 | 11.93 | 14.73 | 14.35 | 11.03 | 5.60 | 13.20 | – | 11.44 | 11.14 |
| $Na_2O$ | 1.99 | 2.16 | 2.38 | 4.12 | 3.03 | 1.25 | 2.07 | 1.64 | 0.36 | 3.08 | – | 2.25 | 2.64 |
| $K_2O$ | 0.02 | 0.03 | 0.02 | 0.05 | 0.03 | 0.02 | 0.06 | < MDL | 0.00 | 0.18 | – | 0.02 | 0.03 |
| Mg# | 89.3 | 71.2 | 81.0 | 76.5 | 72.0 | 82.1 | 64.4 | 75.3 | 84.8 | 55.3 | – | 67.2 | 81.9 |
| Li (ppm) | 1.29 | 1.01 | 1.21 | 2.74 | 2.09 | 0.17 | – | 2.41 | 0.88 | 6.18 | – | 0.48 | 0.50 |
| V | 112 | 338 | 327 | 108 | 139 | 139 | – | 643 | 213 | 316 | – | 196 | 140 |
| Ni | 947 | 16.54 | 333 | 105 | 67.0 | 88.0 | – | 30.41 | 1201 | 54.9 | – | 50.5 | 171 |
| Rb | < MDL | – | < MDL | 0.04 | 0.08 | < MDL | – | < MDL | < MDL | < MDL | – | 0.05 | 0.08 |
| Sr | 46.66 | 52.7 | 116 | 55.2 | 33.68 | 41.48 | – | 121 | 6.64 | 71.1 | – | 26.67 | 60.7 |
| Y | 8.04 | 3.99 | 50.4 | 3.30 | 6.69 | 11.69 | – | 87.7 | 16.61 | 15.34 | – | 11.20 | 18.84 |
| Zr | 76.9 | 17.33 | 76.8 | 11.42 | 17.76 | 13.79 | – | 83.8 | 24.71 | 39.19 | – | 29.94 | 30.52 |
| Nb | 249 | – | 0.53 | 0.14 | 0.20 | 0.08 | – | 0.01 | 0.11 | 11.37 | – | 0.19 | 0.23 |
| Ba | 0.03 | – | 0.28 | 0.04 | < MDL | 0.04 | – | 0.36 | 0.01 | < MDL | – | 0.03 | 0.20 |
| La | 1.73 | 1.19 | 3.57 | 0.35 | 0.28 | 0.56 | – | 2.80 | 0.11 | 0.11 | – | 0.28 | 1.80 |
| Ce | 4.53 | 3.34 | 9.46 | 1.48 | 1.21 | 2.34 | – | 9.05 | 0.51 | 0.60 | – | 1.24 | 4.76 |
| Pr | 0.60 | 0.47 | 1.29 | 0.27 | 0.25 | 0.40 | – | 1.60 | 0.10 | 0.14 | – | 0.25 | 0.63 |
| Nd | 2.96 | 2.40 | 6.16 | 1.53 | 1.59 | 2.12 | – | 9.57 | 0.66 | 1.22 | – | 1.61 | 3.02 |
| Sm | 0.89 | 0.55 | 2.10 | 0.45 | 0.60 | 0.63 | – | 3.57 | 0.43 | 1.11 | – | 0.75 | 0.93 |
| Eu | 0.28 | 0.18 | 0.90 | 0.18 | 0.26 | 0.25 | – | 1.44 | 0.20 | 0.46 | – | 0.31 | 0.38 |

**Table 1** (continued)

| A–B–C type | A | B | B | B | B | A | B | A | A | B | | B | B |
|---|---|---|---|---|---|---|---|---|---|---|---|---|---|
| Gd | 1.04 | 0.57 | 3.81 | 0.54 | 0.86 | 1.00 | – | 6.91 | 1.05 | 2.05 | – | 1.15 | 1.62 |
| Tb | 0.18 | 0.10 | 0.88 | 0.09 | 0.15 | 0.21 | – | 1.61 | 0.27 | 0.38 | – | 0.23 | 0.34 |
| Dy | 1.38 | 0.69 | 7.46 | 0.61 | 1.17 | 1.86 | – | 14.19 | 2.44 | 2.77 | – | 1.79 | 2.91 |
| Ho | 0.31 | 0.16 | 1.94 | 0.13 | 0.25 | 0.45 | – | 3.35 | 0.64 | 0.60 | – | 0.43 | 0.70 |
| Er | 0.95 | 0.54 | 6.31 | 0.38 | 0.79 | 1.48 | – | 10.34 | 2.11 | 1.73 | – | 1.43 | 2.35 |
| Tm | 0.15 | 0.08 | 1.02 | 0.06 | 0.12 | 0.21 | – | 1.59 | 0.33 | 0.25 | – | 0.23 | 0.39 |
| Yb | 1.01 | 0.61 | 7.30 | 0.39 | 0.86 | 1.48 | – | 10.70 | 2.33 | 1.69 | – | 1.63 | 2.58 |
| Lu | 0.15 | 0.10 | 1.14 | 0.06 | 0.13 | 0.24 | – | 1.65 | 0.35 | 0.25 | – | 0.27 | 0.39 |
| Hf | 1.76 | 0.79 | 1.48 | 0.40 | 0.51 | 0.42 | – | 1.75 | 0.52 | 1.39 | – | 0.90 | 0.67 |
| Ta | 9.46 | 0.02 | 0.05 | 0.02 | 0.03 | 0.01 | – | 0.00 | 0.00 | 0.66 | – | 0.03 | 0.02 |
| Pb | 0.07 | 0.06 | 0.61 | 0.05 | 0.03 | 0.04 | – | 0.70 | 0.02 | 0.06 | – | 0.02 | 0.35 |
| Zr/Hf | 43.74 | 21.98 | 52.0 | 28.87 | 34.54 | 32.93 | – | 47.90 | 47.25 | 28.27 | – | 33.30 | 45.81 |
| La/Lu | 11.18 | 12.41 | 3.12 | 6.01 | 2.12 | 2.37 | – | 1.70 | 0.32 | 0.46 | – | 1.06 | 4.59 |
| Yb/Dy | 0.74 | 0.89 | 0.98 | 0.64 | 0.73 | 0.79 | – | 0.75 | 0.95 | 0.61 | – | 0.91 | 0.89 |
| Ce/Yb | 4.48 | 5.46 | 1.29 | 3.75 | 1.41 | 1.59 | – | 0.85 | 0.22 | 0.35 | – | 0.76 | 1.85 |
| Sr/Y | 5.80 | 13.19 | 2.31 | 16.72 | 5.04 | 3.55 | – | 1.37 | 0.40 | 4.63 | – | 2.38 | 3.22 |

| Sample | CH-S9 | CH-S7 | CH-S14 | CH-D19-162 | CH-D19-175 | CH-D15 |
|---|---|---|---|---|---|---|
| Min. a | Ky | Rt | Bimin | Rt | Rt-Opx | Bimin |
| Ecl. Type | – | L-dep. | H-en. | Met | L-dep. | – |
| Cpx | 0.35 | 0.49 | 0.43 | 0.65 | 0.19 | 0.75 |
| Grt | 0.45 | 0.49 | 0.57 | 0.33 | 0.70 | 0.25 |
| Opx | – | – | – | – | 0.09 | – |
| Rt | – | 0.02 | – | 0.02 | 0.02 | – |
| Ky | 0.20 | – | – | – | – | – |

| A–B–C type | | B | B | A | B | B |
|---|---|---|---|---|---|---|
| $SiO_2$ (wt%) | – | 46.54 | 47.99 | 49.48 | – | 52.13 |
| $TiO_2$ | – | 2.17 | 0.37 | 2.02 | – | 0.46 |
| $Al_2O_3$ | – | 16.72 | 15.85 | 10.79 | – | 11.10 |
| $Cr_2O_3$ | – | 0.00 | 0.11 | 0.12 | – | 0.05 |
| FeO | – | 10.14 | 7.82 | 5.75 | – | 7.28 |
| MnO | – | 0.14 | 0.21 | 0.09 | – | 0.19 |
| MgO | – | 8.26 | 17.82 | 14.92 | – | 14.54 |
| CaO | – | 12.51 | 8.31 | 14.71 | – | 10.14 |
| $Na_2O$ | – | 3.23 | 1.77 | 1.75 | – | 4.01 |
| $K_2O$ | – | 0.03 | 0.02 | 0.05 | – | 0.02 |

**Table 1** (continued)

| A–B–C type | | B | B | A | B | B |
|---|---|---|---|---|---|---|
| Mg# | – | 59.2 | 80.2 | 82.2 | – | 78.1 |
| Li (ppm) | – | 19.4 | 0.26 | 2.89 | 3.67 | – |
| V | – | 311 | 82.1 | 89.9 | – | – |
| Ni | – | 64.6 | 66.9 | 104 | – | – |
| Rb | – | 0.21 | < MDL | < MDL | – | – |
| Sr | – | 62.1 | 20.68 | 409 | 35.89 | – |
| Y | – | 12.19 | 14.82 | 2.51 | 11.69 | – |
| Zr | – | 12.02 | 18.18 | 16.85 | 22.66 | – |
| Nb | – | < MDL | 0.11 | 13.70 | – | – |
| Ba | – | < MDL | 0.05 | 0.10 | – | – |
| La | – | 0.13 | 0.62 | 1.12 | 0.17 | – |
| Ce | – | 0.67 | 1.72 | 4.11 | 0.78 | – |
| Pr | – | 0.18 | 0.24 | 0.67 | 0.21 | – |
| Nd | – | 1.43 | 1.18 | 3.55 | 2.21 | – |
| Sm | – | 1.19 | 0.47 | 0.72 | 1.43 | – |
| Eu | – | 0.63 | 0.21 | 0.30 | 0.75 | – |
| Gd | – | 1.87 | 0.95 | 0.54 | 1.92 | – |
| Tb | – | 0.34 | 0.22 | 0.08 | 0.36 | – |
| Dy | – | 2.31 | 2.15 | 0.51 | 2.34 | – |
| Ho | – | 0.46 | 0.55 | 0.10 | 0.47 | – |
| Er | – | 1.34 | 1.95 | 0.27 | 1.28 | – |
| Tm | – | 0.19 | 0.34 | 0.04 | 0.16 | – |
| Yb | – | 1.18 | 2.50 | 0.27 | 1.11 | – |
| Lu | – | 0.18 | 0.42 | 0.04 | 0.16 | – |
| Hf | – | 0.35 | 0.27 | 0.59 | 0.66 | – |
| Ta | – | < MDL | 0.01 | 0.26 | 4.03 | – |
| Pb | – | 0.09 | 0.11 | 0.90 | 0.04 | – |
| Zr/Hf | – | 34.14 | 66.64 | 28.45 | 34.54 | – |
| La/Lu | – | 0.69 | 1.49 | 27.20 | 1.02 | – |
| Yb/Dy | – | 0.51 | 1.16 | 0.54 | 0.47 | – |
| Ce/Yb | – | 0.57 | 0.69 | 15.04 | 0.71 | – |
| Sr/Y | – | 5.10 | 1.40 | 163 | 3.07 | – |

$Mg\# = 100 \times Mg/(Mg + Fe^{total})$ molar

*Min. a.* mineral association (minor and/or accessory minerals), *Bimin* bimineral eclogites (Grt and Cpx), *Rt* bimineral eclogites with accessory rutile, *Ky* kyanite-bearing eclogites, *Opx-Rt* orthopyroxene-bearing eclogites with accessory rutile. A–B–C type, after Taylor and Neal (1989). – not applicable/not measured, < *MDL* less than the minimum detection limit, *Ecl. Type* (eclogite types): *H-en.* HREE-enriched, *L-dep.* LREE-depleted, *Met*. metasomatized eclogite

**Table 2** Major element composition of garnet and clinopyroxene from the representative Chidliak eclogites (wt%)

| Sample | Q-A | Q-B | CH-6 | CH-7 | CH-N1 | CH-S3 | CH-S4 | CH-D27-80 | CH-D28 |
|---|---|---|---|---|---|---|---|---|---|
| Min. a | Rt-Opx | Rt | Bimin | Bimin | Bimin | Bimin | Rt | Bimin | Rt-Opx |
| Type | Met | Met | H-en. | Met | L-dep. | H-en. | – | H-en. | L-dep. |
| Garnet | | | | | | | | | |
| N_a | 11 | 1 | 9 | 1 | 2 | 1 | 3 | 10 | 1 |
| $SiO_2$ | 42.68 | 41.23 | 41.92 | 40.38 | 40.49 | 41.40 | 39.31 | 40.90 | 42.37 |
| $TiO_2$ | 0.34 | 0.64 | 0.32 | 0.61 | 0.68 | 0.26 | 0.13 | 0.21 | 0.43 |
| $Al_2O_3$ | 24.12 | 22.63 | 23.61 | 22.81 | 22.64 | 23.20 | 22.52 | 23.43 | 23.74 |
| $Cr_2O_3$ | 0.19 | < MDL | < MDL | 0.38 | 0.36 | 0.16 | < MDL | 0.13 | 0.18 |
| FeO | 7.55 | 15.23 | 10.55 | 13.83 | 13.09 | 11.09 | 20.68 | 14.72 | 8.25 |
| MnO | 0.36 | 0.43 | 0.30 | 0.31 | 0.30 | 0.35 | 0.42 | 0.36 | 0.34 |
| MgO | 21.95 | 15.24 | 20.10 | 14.10 | 13.26 | 17.62 | 9.18 | 16.94 | 21.25 |
| CaO | 3.41 | 5.17 | 2.96 | 8.06 | 9.14 | 5.82 | 7.95 | 3.66 | 3.68 |
| $Na_2O$ | 0.10 | 0.15 | 0.12 | 0.20 | 0.21 | 0.06 | 0.07 | 0.07 | 0.09 |
| Total | 100.70 | 100.72 | 99.88 | 100.68 | 100.17 | 99.96 | 100.26 | 100.42 | 100.33 |
| Clinopyroxene | | | | | | | | | |
| N_a | 10 | 1 | 8 | 9 | 1 | 16 | 27 | 2 | 3 |
| $SiO_2$ | 54.84 | 55.75 | 55.08 | 54.65 | 54.65 | 54.58 | 54.79 | 55.59 | 55.11 |
| $TiO_2$ | 0.38 | 0.49 | 0.48 | 0.53 | 0.48 | 0.23 | 0.14 | 0.25 | 0.22 |
| $Al_2O_3$ | 3.91 | 5.54 | 5.22 | 8.63 | 8.63 | 2.73 | 5.12 | 4.23 | 2.74 |
| $Cr_2O_3$ | 0.14 | < MDL | 0.07 | 0.36 | 0.30 | 0.15 | < MDL | 0.14 | 0.26 |
| FeO | 2.79 | 5.91 | 4.30 | 4.15 | 4.22 | 3.62 | 5.48 | 3.70 | 2.96 |
| MnO | 0.08 | 0.10 | 0.08 | < MDL | < MDL | < MDL | < MDL | < MDL | 0.08 |
| MgO | 15.83 | 13.08 | 14.42 | 10.91 | 10.66 | 15.74 | 12.39 | 14.50 | 17.09 |
| CaO | 18.43 | 15.66 | 15.40 | 14.27 | 14.22 | 20.72 | 18.53 | 18.40 | 19.43 |
| $Na_2O$ | 2.97 | 3.88 | 4.15 | 5.29 | 5.33 | 2.01 | 3.30 | 3.21 | 1.91 |
| $K_2O$ | 0.03 | 0.05 | 0.04 | 0.06 | 0.05 | 0.03 | 0.09 | < MDL | 0.02 |
| Total | 99.40 | 100.46 | 99.24 | 98.85 | 98.54 | 99.81 | 99.84 | 100.02 | 99.82 |

| Sample | CH-D27-184 | CH-S10 | CH-S13 | CH-S7 | CH-S14 | CH-D19-162 | CH-D19-175 |
|---|---|---|---|---|---|---|---|
| Min. a | Rt | Bimin | Bimin | Rt | Bimin | Rt | Rt-Opx |
| Type | L-dep. | L-dep. | H-en. | L-dep. | H-en. | Met | L-dep. |
| Garnet | | | | | | | |
| N_a | 1 | 5 | 3 | 2 | 1 | 4 | 15 |
| $SiO_2$ | 38.63 | 40.22 | 42.29 | 39.19 | 42.12 | 41.15 | 39.58 |
| $TiO_2$ | 0.48 | 0.90 | 0.36 | 0.17 | 0.31 | 0.09 | 0.16 |
| $Al_2O_3$ | 21.94 | 22.11 | 23.74 | 22.85 | 23.83 | 23.46 | 22.99 |
| $Cr_2O_3$ | < MDL | < MDL | 0.13 | < MDL | 0.11 | 0.13 | < MDL |
| FeO | 22.48 | 15.17 | 10.58 | 17.14 | 10.50 | 12.45 | 13.67 |
| MnO | 0.41 | 0.33 | 0.34 | 0.28 | 0.32 | 0.26 | 0.34 |
| MgO | 6.90 | 13.00 | 20.21 | 8.15 | 20.28 | 16.53 | 9.32 |
| CaO | 9.80 | 8.23 | 2.99 | 12.19 | 2.91 | 5.88 | 13.97 |
| $Na_2O$ | 0.17 | 0.22 | 0.13 | 0.14 | 0.10 | 0.05 | 0.09 |
| Total | 100.81 | 100.18 | 100.77 | 100.11 | 100.48 | 100.00 | 100.12 |
| Clinopyroxene | | | | | | | |
| N_a | 5 | 10 | 5 | 3 | 11 | 4 | 12 |
| $SiO_2$ | 54.08 | 55.03 | 55.79 | 55.79 | 55.78 | 55.23 | 56.12 |
| $TiO_2$ | 0.37 | 0.63 | 0.46 | 0.18 | 0.45 | 0.09 | 0.14 |
| $Al_2O_3$ | 7.55 | 6.91 | 5.22 | 11.27 | 5.28 | 4.68 | 10.61 |
| $Cr_2O_3$ | < MDL | < MDL | 0.14 | < MDL | 0.11 | 0.10 | < MDL |

**Table 2** (continued)

| Sample | CH-D27-184 | CH-S10 | CH-S13 | CH-S7 | CH-S14 | CH-D19-162 | CH-D19-175 |
|---|---|---|---|---|---|---|---|
| Min. a | Rt | Bimin | Bimin | Rt | Bimin | Rt | Rt-Opx |
| Type | L-dep. | L-dep. | H-en. | L-dep. | H-en. | Met | L-dep. |
| FeO | 7.81 | 5.53 | 4.34 | 3.55 | 4.26 | 2.49 | 2.37 |
| MnO | 0.08 | 0.07 | 0.08 | < MDL | 0.07 | < MDL | < MDL |
| MgO | 9.27 | 11.73 | 14.55 | 8.70 | 14.56 | 14.56 | 10.07 |
| CaO | 15.09 | 15.37 | 15.53 | 13.34 | 15.46 | 19.65 | 15.03 |
| $Na_2O$ | 4.46 | 4.73 | 3.99 | 6.45 | 3.98 | 2.66 | 5.48 |
| $K_2O$ | 0.27 | 0.04 | 0.04 | 0.07 | 0.04 | 0.08 | 0.07 |
| Total | 98.98 | 100.04 | 100.14 | 99.35 | 99.99 | 99.54 | 99.89 |

*N_a* number of analyses averaged, – not applicable/not measured, <*MDL* less than the minimum detection limit, *Min. a* mineral assemblages, *Bimin* bimineralic eclogite (garnet and clinopyroxene), *Rt* bimineralic eclogite with rutile (up to 3 modal%), *Ky* kyanite eclogite, *Rt-Opx* rutile–orthopyroxene eclogite. Types: *H-en.* HREE-enriched, *L-dep.* LREE-depleted, *Met* metasomatized

There is no significant difference between eclogite groups in Li, V, Ni, Sr, Zr, Nb, Ba, Hf, Ta and Pb contents (Table 1; Online Resource 4). Yttrium concentrations in the metasomatized eclogites are slightly lower (0.6–1.9 ppm) in comparison with the HREE-enriched (2.7–20.4 ppm) and the LREE-depleted (1.6–3.9 ppm) eclogites.

## Major and trace element composition of minerals

### Garnet

Garnets from the Chidliak eclogites show a wide variation in composition (Table 2) ranging from 26.9 to 76.5% pyrope [Prp], 14.6–49.2% almandine [Alm] and 5.0–50.5% grossular [Grs]. The sum of the other end-members (Spessartine, Uvarovite and Schorlomite) varies from 0.2 to 2.8%. Garnet from the single kyanite eclogite has the most grossular-rich composition Prp34 Alm15 Grs51 (Fig. 3). Garnet from the metasomatized eclogites is pyrope-rich with compositions Prp52–76 Alm15–32 Grs7–16 (Fig. 3). HREE-enriched eclogites also contain pyrope-rich garnet with similar composition Prp62–72 Alm21–30 Grs6–12. Garnet from LREE-depleted eclogites is represented by pyrope (3 samples), almandine (2 samples) and grossular (1 sample), i.e., Prp27–75 Alm16–49 Grs7–37.

REE and trace element compositions of garnets show significant variations. REE patterns have been subdivided into four types based on $Sm_N/Yb_N$: (a) inclined, most common patterns with $Sm_N/Yb_N$ of 0.1–0.4 (type I pattern according to Jacob 2004) (Fig. 4a); (b) flattened patterns with a positive MREE to HREE slope ($Sm_N/Yb_N = 0.5$) (Fig. 4b). LREE contents in these garnets are the same as in the "a" patterns, but HREE concentrations are strongly (up to 8 times) depleted; (c) flattened patterns with a negative MREE to HREE slope and a positive Eu anomaly ($Sm_N/Yb_N = 0.9–1.3$, $Eu/Eu^* = 1.3–1.6$) (type II pattern according to Jacob 2004) (Fig. 4c); (d) a REE pattern with slightly enriched LREE, strongly depleted MREE and relatively low HREE. Thus, the shape of the pattern is close to a straight line (Fig. 4d). Garnets from the HREE-enriched eclogites exhibit only the inclined patterns, garnets from the LREE-depleted eclogites show (a), (b) and (c) types of REE patterns; whereas, garnet from the metasomatized eclogites exhibit all REE types. Garnet eclogitic inclusions in Chidliak diamonds (Xia 2018) belong to (c) and (d) types of REE patterns (Fig. 4).

Other trace elements vary in a wide range, 317–3830 ppm of Na, 511–9862 ppm of Ti, 7–169 ppm of Y and 8–133 ppm of Zr, but correlations between their abundances and the type of REE pattern or the type of eclogite were not found.

### Clinopyroxene

Most clinopyroxene (Mg# = 68–91) is represented by omphacite (Table 2; Fig. 5a) with 13.2–45.3% Jadeite [Jd], 0.0–9.3% Aegirine [Aeg], and 54.7–79.1% quadrilateral pyroxene [Quad] end-members (hereafter Quad is Enstatite [En] + Ferrosilite [Fs] + Wollastonite [Wo]). All clinopyroxenes belong to A and B groups according to the A–B–C eclogite classification of Taylor and Neal (1989). Moreover, each group comprises metasomatized, HREE-enriched and LREE-depleted eclogites (Fig. 5b). Four HREE-enriched eclogites have omphacite with a narrow range of jadeite end-member, Jd18–23 Aeg4–9 Quad71–78, and one HREE-enriched sample CH-D19-162 contains Al-sodian diopside. Omphacite from the LREE-depleted eclogites is more jadeitic (Jd27–45 Aeg < 6 Quad55–68), showing less magnesian compositions than omphacite from the HREE-enriched eclogites (the average Mg# values of 82 vs. 87) (Fig. 5). Metasomatized eclogites contain omphacite or chromian omphacite (sample CH-7 with 0.36 wt% of $Cr_2O_3$) with a

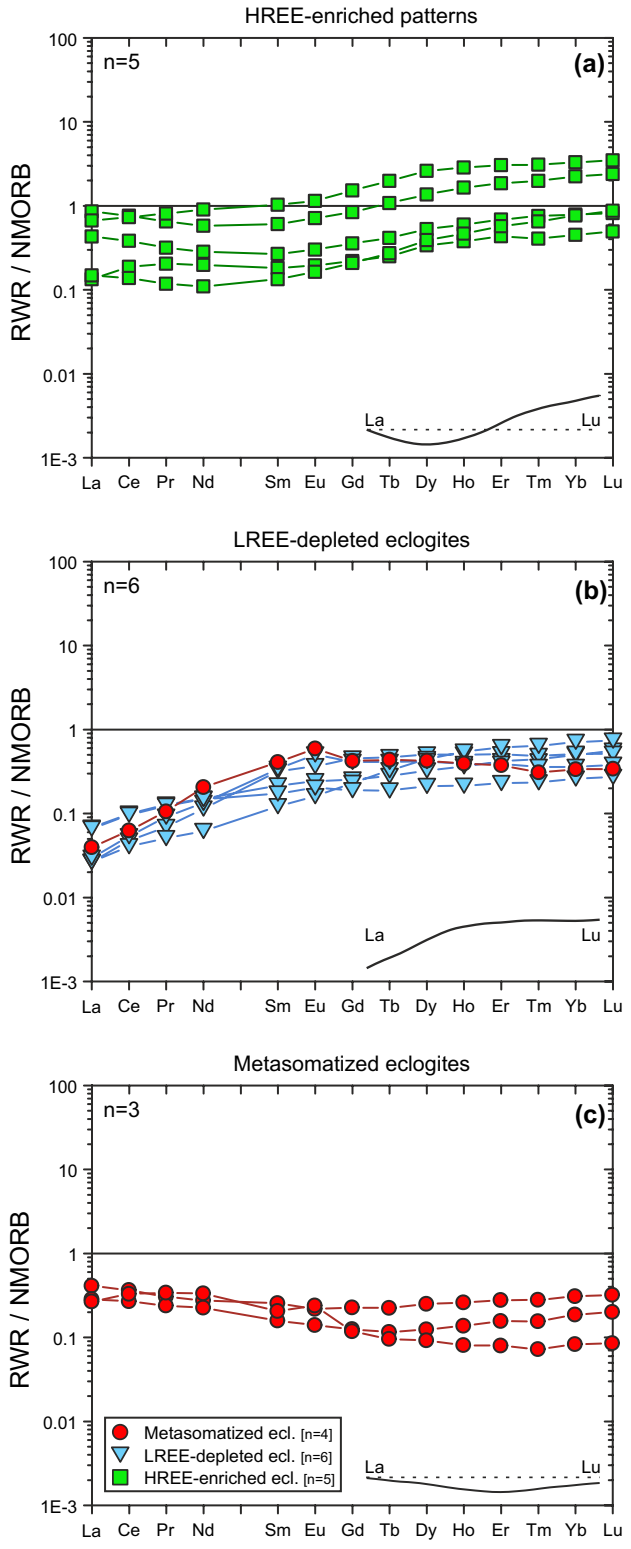


**Fig. 2** Classification of the Chidliak eclogites into three groups: (**a**) HREE-enriched, (**b**) LREE-depleted and (**c**) metasomatized, based on NMORB-normalized REE patterns of the reconstructed whole-rock (RWR) compositions. NMORB values are after Gale et al. (2013). The La-Lu profiles on the right bottom corner approximate the shapes of the REE diagrams

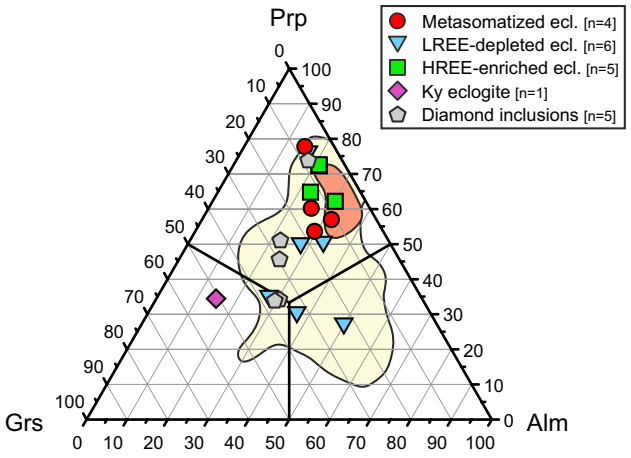


**Fig. 3** Ternary diagram [Pyrope (Prp)-Almandine (Alm)-Grossular (Grs)] showing the end-member composition of garnet from the Chidliak mantle eclogites. The sum of these end-members ranges from 97.2 to 99.8% (Online Resource 1). End-members are calculated according to the method proposed by Arai (2010). The yellow field corresponds to garnets from Slave eclogites and eclogitic garnet inclusions from diamonds (Prp + Alm + Grs > 95%) ($n = 384$, Online Resource 5) and red field—to NAC eclogites ($n = 11$, Tappe et al. 2011). Compositions of the Chidliak diamond inclusions are from Xia (2018)

wide variation of jadeite end-member, Jd13–35 Aeg1–8 Quad 63–79. Clinopyroxene shows a wide variation of some trace elements (Table 2), e.g., 0.1–38.3 ppm of Li, 22–1392 ppm of K, 55–517 ppm of V, 42–629 ppm of Sr and 1.8–53.5 ppm of Zr. Correlations between the element concentrations and the type of eclogite were not found. REE patterns of clinopyroxene from all types of the Chidliak eclogites are similar, with the relatively high LREE and low HREE contents and $La_N/Er_N$ of 6.3–16.6 (Fig. 5c).

## Accessory and secondary minerals

Rutile shows relatively constant composition, with low contents of $Nb_2O_5$ (<1.8 wt%), FeO (tot) (<1.1 wt%) and $Cr_2O_3$ (<0.5 wt%) irrespective of the eclogite type. The highest variations are seen for Nb (568–12,440 ppm), Zr (621–2849 ppm), Ta (13–473 ppm) and Ni (2.8–41.4 ppm). Ilmenite exsolution lamellae in rutile vary extensively in FeO content (29.3–40.3 wt%) and MgO (4.0–12.4 wt%). Small size of the lamellae (<15 μm wide) did not allow trace element analysis.

Orthopyroxene is enstatite (En92–93 Fs7–8 Wo < 1) with Mg# of 93 and very low REE contents.

Secondary clinopyroxene is invariably less jadeitic, Jd 7–35 compared to Jd 12–46 for primary clinopyroxene (Fig. 5), but both types of clinopyroxene are stoichiometric, with cations totals of 4.00 and charge balance of 12.00 (Online Resource 1).

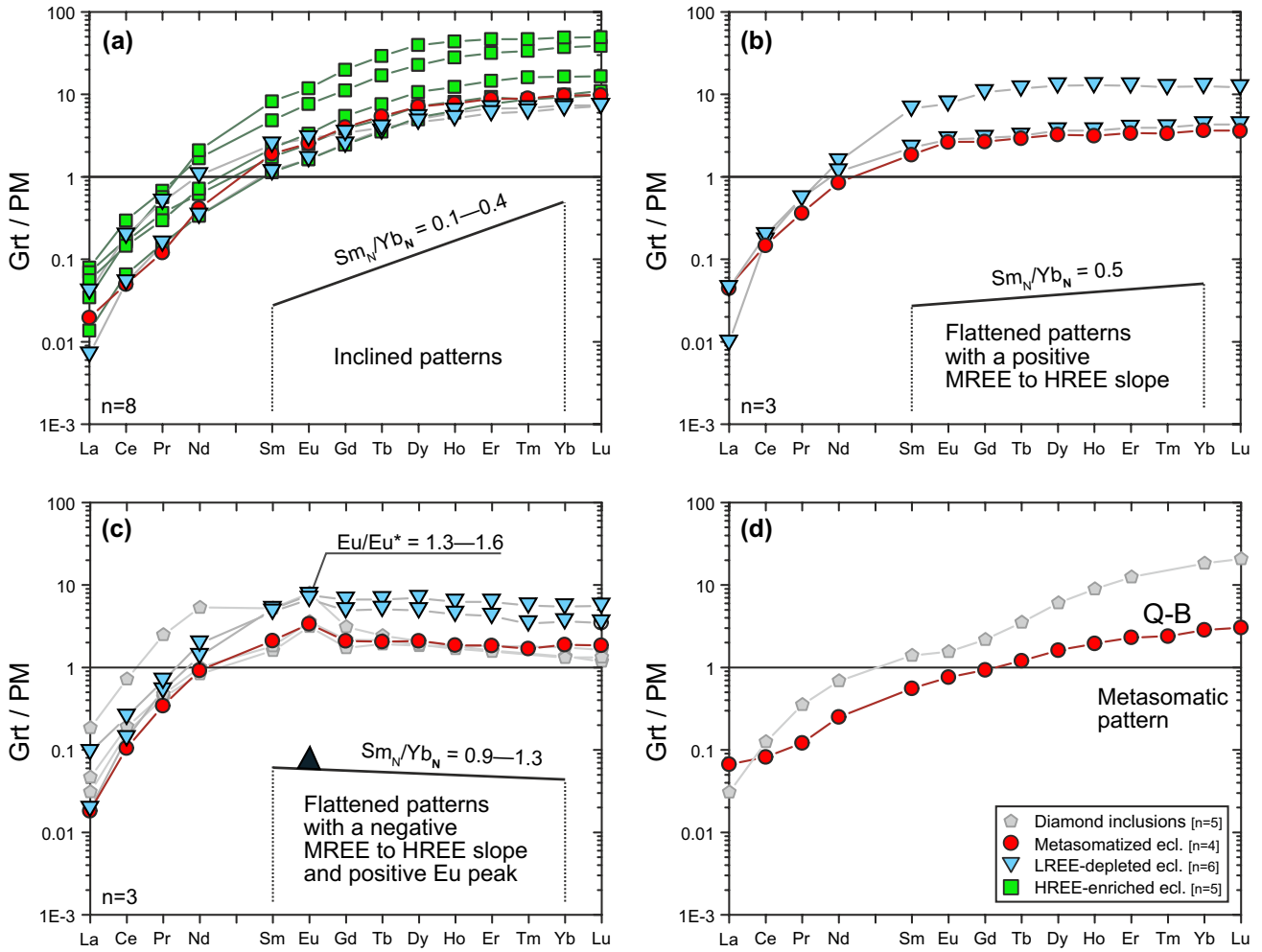


**Fig. 4** Primitive-mantle-normalized REE patterns of garnet. **a** Inclined REE patterns with $Sm_N/Yb_N$ of 0.1–0.4. **b** Flattened patterns with a positive MREE to HREE slope. **c** Flattened patterns with a negative MREE to HREE slope and a positive Eu anomaly. **d** Strongly metasomatized sample (Q-B) showing REE pattern with slightly enriched LREE, strongly depleted MREE and relatively low HREE. The Sm–Yb profiles on the right bottom corner approximate the shapes of the REE patterns. Compositions of the Chidliak diamond inclusions are from Xia (2018). Primitive mantle values from McDonough and Sun (1995)

Phlogopite with composition $Phlogopite_{80–94}Annite_{6–20}$ was found in 8 out of 19 samples. Pargasite amphibole occurs in 10 out of 19 samples, with a range of compositions $K_{0.15–0.32}$ $Na_{0.71–0.88}$ ($Na_{0–0.21}$ $Ca_{1.45–1.74}$ $Mg_{0.20–0.46}$) [$Mg_{2.94–3.54}$ $Fe_{0.77–1.79}$ $Ti_{0.03–0.30}$ $Al_{0.50–1.30}$] [$Si_{5.77–6.11}$ $Al_{1.90–2.30}$] $O_{22}$ $(OH)_2$.

## Thermobarometry

Equilibration pressures ($P$) and temperatures ($T$) of the eclogites were obtained using the latest version of the garnet–clinopyroxene geothermometer (Nakamura 2009) in combination with local geotherms derived for 65 peridotite xenoliths from Chidliak (Kopylova et al. 2019). This methodology is based on the assumption of thermal equilibration between eclogites and peridotites, the texturally equilibrated metamorphic rocks residing for billions of years together at $T = 800–1300$ °C. The Chidliak peridotite arrays were constructed using the Taylor (1998) two-pyroxene thermometer combined with the Nickel and Green (1985) orthopyroxene–garnet barometer for lherzolites. For harzburgites, the latter barometer was paired with the orthopyroxene–garnet thermometer of Nimis and Grütter (2010). This combination of a barometer with two thermometers is considered accurate to ± 50 °C (1σ) and ± 0.25 GPa (1σ) (Nimis and Grütter 2010). The internal consistency of the peridotite thermobarometry with the Nakamura (2009) thermometer has not been ascertained, but the calibrations have been proven accurate for the corresponding rock types empirically and experimentally (Nickel and Green 1985; Nimis and Grütter 2010; Taylor 1998).

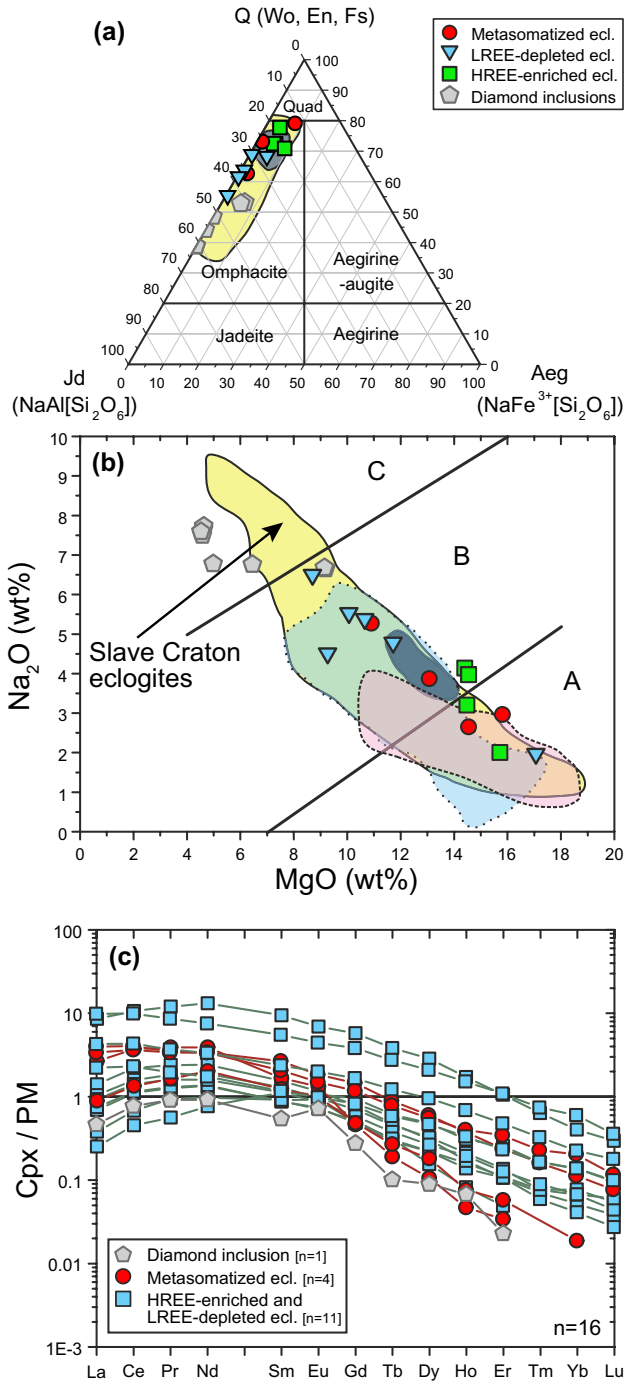


**Fig. 5** Compositions of clinopyroxene from the Chidliak eclogites. **a** End-member compositions (Aeg, aegirine, En, enstatite, Fs, ferrosilite, Jd, jadeite and Wo, wollastonite) of the studied clinopyroxene on the classification diagram of Morimoto (1988). End-members are calculated using the PX-NOM program (Sturm 2002). **b** The $Na_2O$-MgO compositions of clinopyroxenes in comparison with the A–B–C eclogitic classification (Taylor and Neal 1989). Yellow field corresponds to clinopyroxene from Slave eclogites ($n=282$), blue field to Slave eclogitic diamond inclusions (DI) ($n=39$, Online Resource 5), red field to secondary clinopyroxene from the studied Chidliak eclogites ($n=28$) and black field to NAC mantle eclogites ($n=11$, Tappe et al. 2011). Note, that clinopyroxene inclusions from the E-type Chidliak diamonds (Xia 2018) are significantly more jadeitic, less magnesian and belong overwhelmingly to Group C. **c** Primitive mantle normalized REE patterns of clinopyroxenes. Compositions of eclogitic inclusions from the Chidliak diamonds are from Xia (2018). Primitive mantle values from McDonough and Sun (1995)

Projection of garnet–clinopyroxene eclogite temperatures onto the Chidliak peridotitic *P–T* arrays can be done in different ways, as the latter do not conform to the shape of model conductive geotherms and scatter in the *P–T* space with geotherms corresponding to a surface heat flow between 33 and 39 mW/m$^2$ (Hasterok and Chapman 2011) (Fig. 6; Online Resource 6). Therefore, we projected the eclogitic temperatures onto a variety of approximated *P–T* lines (Online Resource 6), which we call for simplicity "geotherms", although their conductive origin cannot be ascertained. We used the following geotherms: (1) modeled for 35, 36, 37, 38, 39 and 40 mW/m$^2$ surface heat flows (Hasterok and Chapman 2011); (2) derived as a linear fit for CH-6 peridotites and CH-1, -7, -44 peridotites separately; (3) derived for CH-6 peridotites and CH-1, -7, -44 peridotites separately using the FITPLOT methodology of Mather et al. (2011), which makes geotherms for the specified crust and upper crust thicknesses and heat production; (4) derived as a linear fit for all Chidliak peridotites together; (5) derived for all Chidliak peridotites using the FITPLOT methodology of Mather et al. (2011).

The difference between calculated Chidliak eclogite temperatures, when projected onto a linear fit-averaged geotherm, and the linear fit geotherms for CH-6 peridotites and CH-1, -7, -44 peridotites separately, is >41 °C (Online Resource 6). This is significantly less than the 1-sigma standard deviation of 74 °C for the Nakamura (2009) thermometer. The similar difference in temperatures (<43 °C) was obtained from a comparison of the averaged Chidliak peridotite geotherm by Mather et al. (2011) and the geotherm calculated from the linear approximation of all the peridotites. It would be less accurate to project eclogitic temperatures to model geotherms (Hasterok and Chapman 2011). Therefore, for further discussion, we chose *P–T* values yielded by intersecting eclogitic univariant *P–T* lines with the Mather et al. (2011) geotherm for all Chidliak peridotites.

Chidliak eclogites formed over a significant range of PT values, from 842 °C at 4.1 GPa up to adiabatic *P–T* conditions of 1412 °C at 6.5 GPa (Fig. 6). These calculated temperatures are within the range of experimental calibration temperatures (800–1820 °C) of Nakamura (2009). There are two main groups of eclogites, low-temperature eclogites (5 out of 16) with PT-parameters of 842–988 °C at 4.1–5.0 GPa and high-temperature eclogites with PT-parameters of >1320 °C at > 7.0 GPa (8 out of 16) (Fig. 6). Three samples from the latter group have super-adiabatic temperatures and were projected onto an ambient mantle adiabat with the potential temperature of 1327 ± 40 °C (Katsura et al. 2010). A link between the eclogite type and PT-parameters was not found. Both low- and high-temperature eclogites comprise samples belonging to the metasomatized, LREE-depleted and HREE-enriched eclogites. Another suite

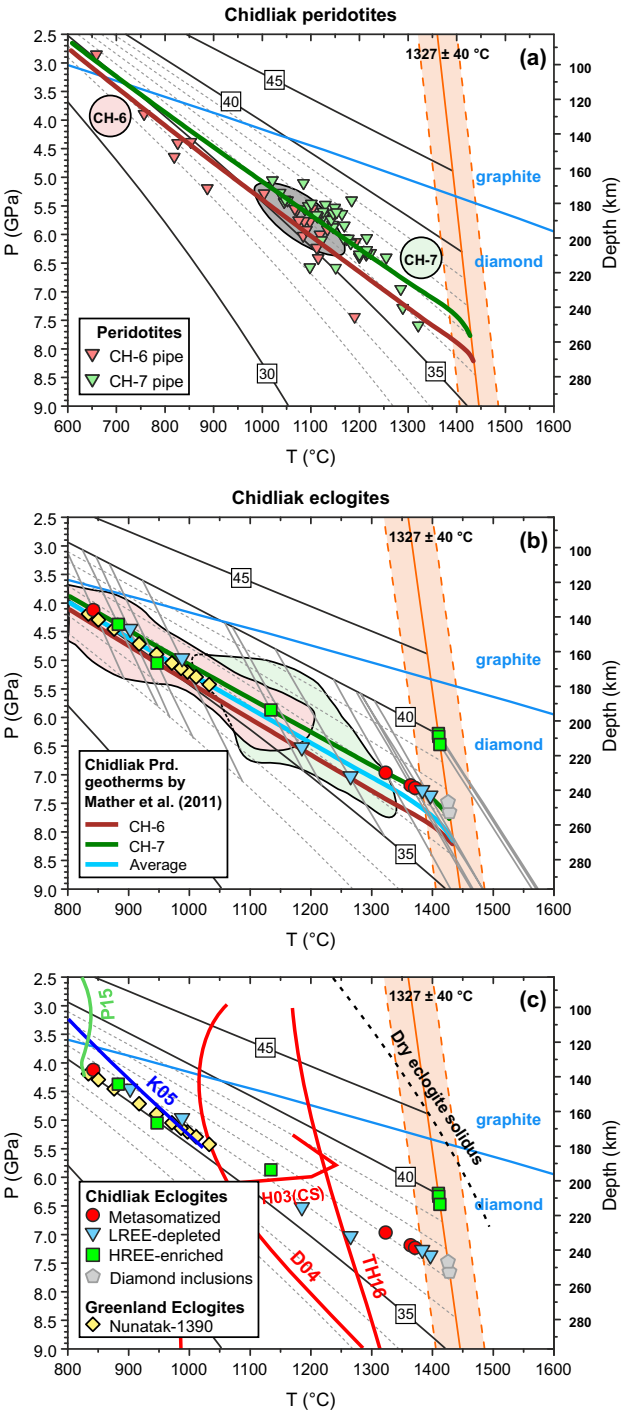


**Fig. 6** Pressure–temperature estimates for (**a**) the studied Chidliak mantle peridotites (Kopylova et al. 2019) and (**b**) eclogites [this study and the Greenland eclogites (Tappe et al. 2011)]. Model conductive geotherms labeled 30, 35, 40 and 45 mW/m$^2$ or given by the gray dotted lines (33, 34, 36, 37, 38 and 39 mW/m$^2$) are after (Hasterok and Chapman 2011); they terminate at an ambient mantle adiabat with a potential temperature of 1327 ± 40 °C and temperature gradient of 0.4 °C/km (Katsura et al. 2010). Dashed lines parallel to the adiabat show the 40 °C uncertainty of the ambient adiabat. The graphite–diamond phase boundary of Day (2012) is shown by the dark blue line. **a** Pressure–temperature estimates for the Chidliak mantle peridotites (Kopylova et al. 2019), and CH-6 and CH-7 peridotite geotherms calculated using FITPLOT (Mather et al. 2011). Gray field corresponds to the temperatures (985–1170 °C) calculated from the degree of nitrogen aggregation (Taylor et al. 1990; Leahy and Taylor 1997) for the Chidliak diamonds computed for a 2.7 Ga mantle residence time (Xia 2018). **b** Comparison of PT-parameters of the Chidliak eclogites projected onto the Chidliak peridotite geotherms, calculated by FITPLOT (Mather et al. 2011) [green (CH-6) and red lines (CH-1, -7, -44)], and peridotites from CH-6 (red field) and CH-1, -7, -44 (green field) pipes. The blue line is the averaged peridotite geotherm. PT-parameters of the Chidliak eclogites projected onto the peridotite geotherms (CH-6 and CH-1, -7, -44) and 35, 36, 37, 38, 39 and 40 conductive geotherms after (Hasterok and Chapman 2011) are given in Online Resource 6. Curves of geotherms by Mather et al. (2011) can be approximated in the interval 600–1400 °C using quadratic equations ($R$-Square > 0.999): for CH-6 peridotites P(GPa) = (−14.8 1092 + 0.07322 × $T$(°C) − 4.51215E−6 × $T$(°C)$^2$)/10, for CH-1, -7, -44 peridotites P(GPa) = (−13.7871 + 0.06922 × $T$(°C) − 4.67171 E−6 × $T$(°C)$^2$)/10 and the averaged geotherm P(GPa) = (−13.2103 + 0.06868 × $T$(°C) − 3.24716E−6 × $T$(°C)$^2$)/10. The semi-transparent red field denotes PT-parameters of CH-6 peridotites, the green field—PT-parameters of CH-1, -7, -44 peridotites. *P–T* estimates for Chidliak diamond inclusion pairs were computed based on Nakamura (2009) temperatures intersected with the Chidliak geotherm for diamond inclusion compositions of Xia (2018). **c** PT-parameters of the NAC mantle eclogites [metasomatized, LREE-depleted and HREE-enriched eclogites from this work and Greenland eclogites after Tappe et al. (2011)] in comparison with the eclogite solidi positions ( modified from Elazar et al. 2019). Dry eclogite solidus after (Yasuda et al. 1994). Red lines represent carbonated eclogite systems: *H03*(*CS*) Hammouda (2003) carbonated eclogite solidus, *D04* Dasgupta et al. (2004), *TH16* Thomson et al. (2016). Green line *P15* hydrous carbonated system after Poli (2015). Blue line *K05* hydrous eclogite solidus (Kessel et al. 2005)

of NAC mantle eclogites from Nunatak-1390 plot with the low-T group (Fig. 6b) when the temperatures are recalculated with the Nakamura (2009) thermometer and projected on the Chidliak peridotitic *P–T* array.

## Discussion

### Comparison of the Chidliak and Nunatak-1390 eclogites

Two groups of NAC mantle eclogites, Chidliak and Nunatak-1390, found under different rifted blocks of the craton, are significantly different. As expected from the more abundant samples at Chidliak, the latter are more diverse, both geochemically and with respect to equilibrium *P–T* conditions. Nunatak-1390 eclogites were divided using the Pb isotopic systematics into "pristine", defining a statistically meaningful Pb–Pb secondary isochron age, and "overprinted", whose Pb isotope compositions and elevated trace elements reflect kimberlite infiltration (Tappe et al. 2011).

Among three groups of Chidliak eclogites, the HREE-enriched eclogites are the closest to the Nunatak-1390 eclogites in terms of major and trace element compositions

(Figs. 7, 8a, 9a), although the HREE-enriched eclogites show wider variations in CaO and $Al_2O_3$ (Fig. 7d, e). Similarly, the HREE-enriched eclogites cover the range of REE contents of "pristine" Nunatak-1390 eclogites, but extend to significantly higher HREE contents in two samples (Figs. 8a, 9a). "Stepped" REE shapes of HREE-enriched eclogites might relate to dehydration in subduction zones (Aulbach et al. 2020). The resemblance of HREE-enriched Chidliak and "pristine" Nunatak-1390 eclogites indicate that conclusions on the origin of the Nunatak-1390 samples from partial melting of seafloor-altered basaltic oceanic crust (Tappe et al. 2011) may be partly extrapolated to the HREE-enriched eclogites. The Chidliak HREE-depleted eclogites may have experienced a lower degree of partial melting, below 10%, matched by less depletion in LREE in comparison to MREE ($La/Eu_N$ 0.6–1.4) (Fig. 8a), than the Nunatak-1390 eclogites ($La/Eu_N$ 0.3–0.7).

The LREE-depleted and metasomatized eclogites show spidergrams different from Nunatak-1390 eclogites (Fig. 9b, c). The LREE-depleted xenoliths are more depleted in LREE, do not have a positive Pb and negative Zr anomalies, and show a positive Sr anomaly (Fig. 9b). Metasomatized eclogites in comparison with the Nunatak-1390 samples exhibit negative Pb (3 out of 4) and positive Sr anomalies with a strong HREE depletion (Fig. 9c). All Chidliak eclogites are enriched in high field strength elements (HFSE, Zr Ti, Hf) compared to the Nunatak-1390 samples (Fig. 9), consistent with the presence of accessory rutile at Chidliak.

The mismatch between the Nunatak-1390 eclogites and LREE-depleted and metasomatized eclogites opens a possibility of their non-basaltic protolith, or a diverging history of partial melting and/or mantle metasomatism. This conclusion is further corroborated by the wider ranges of pressures and temperatures recorded by Chidliak eclogites (Fig. 6b) and their deeper origin with equilibration on a conductive geotherm and on an adiabat.

## Origin of the Chidliak mantle eclogites

We consider the crustal origin of the Chidliak eclogites as the most probable model because: (1) most eclogitic Chidliak diamonds were sourced from isotopically light organic carbon ($< -10$ ‰) correlated with $\delta^{15}$ N ($-1.3$–$7.1$ ‰), which is typical for subducted slabs (Xia 2018); (2) NAC eclogites from Greenland were inferred to have formed from metamorphosed mafic crust (Tappe et al. 2011), and (3) the predominant majority of eclogites under cratons are crustal in origin (e.g., Barth et al. 2001, 2002a; Jacob 2004; Smart et al. 2014; Snyder et al. 1997). Crustal eclogites may be transported into the mantle via different mechanisms, by subduction after 3.0–3.3 Ga or by delamination in the early tectonics (Foley et al. 2003).

Reconstructed REE profiles of Chidliak eclogites attest to a possible residual character of LREE-depleted group of samples as well as the complex, multi-stage formation of all other groups of samples. The LREE-depleted Chidliak eclogites exhibit NMORB-normalized REE patterns with low LREE (0.02–0.15 of the NMORB concentrations) and flat MREE to HREE (0.2–0.9) (Figs. 2b, 8a), indicating extraction of partial melt. Archean cratonic eclogites are commonly viewed as residues after extraction of TTGs (Ireland et al. 1994; Foley et al. 2003; Moyen 2011; Tappe et al. 2011). The REE profiles of the LREE-depleted Chidliak eclogites and the occurrence of Archean TTGs in the EHP (From 2017; From et al. 2018) prompted us to explore their complementarity. As a possible protolith we selected the average NAC Archean basalt, because the C–N isotopic systematics of eclogitic Chidliak diamonds ($\delta^{13}C < -10$ ‰, $\delta^{15}N = -1.3$–$7.1$ ‰) is more likely to be acquired in the upper part of the oceanic crust (Xia 2018). Batch melting modeling at $T = 1200$ °C at 3.0 GPa, i.e., the expected parameters of slab melting (Moyen 2011) for an average NAC Archean basalt composition (based on 132 samples of the NAC Archean basalts and picrites, Online Resource 5) shows that shapes of residual REE patterns after 15–55% partial melting are in excellent agreement with the observed LREE-depleted eclogites patterns (Fig. 10c). Moreover, the REE patterns of melts produced in the course of the melting generally correspond to the average Archean Gray gneiss, average Archean TTG (Moyen and Martin 2012) and TTG rocks from EHP, which are most likely derived from the same Archean crust as the Chidliak eclogites (Fig. 10d). Zr and Hf contents of the RWR eclogite compositions also match the residual compositions after 5–25% partial melting at temperatures of 1200 °C (Fig. 8b). The modeling also narrows down the viable *P*–*T* parameters of melting within a range of possible depths and temperatures expected for Archean slabs (Moyen 2011). Relatively high pressures of melting in the eclogitic facies (3.0 GPa) at temperatures between 1200 and 1400 °C satisfy the observed REE patterns of eclogites and TTGs, but the same degree of melting at the amphibole facies of metamorphism ($T = 1000$ °C at 1.8 GPa) (Moyen 2011) failed the modeling test (Fig. 10a, b). Neither residues nor extracted melts correspond to the LREE-eclogite and EHP TTG compositions respectively, even at the highest degrees of partial melting (Fig 10a, b).

Two samples of the LREE-depleted eclogites possess some distinct geochemical characteristics that point to their residual character after melting of gabbroic protolith. Gabbro, by comparison with basalt, is more likely to involve plagioclase cumulation and, therefore, should display characteristic positive Sr and Eu anomalies and high whole-rock $Al_2O_3$ (e.g., Aulbach and Jacob 2016; Jacob 2004). Two Chidliak eclogites may have formed after a plagioclase-rich protolith of metamorphosed gabbro based on: (1) the

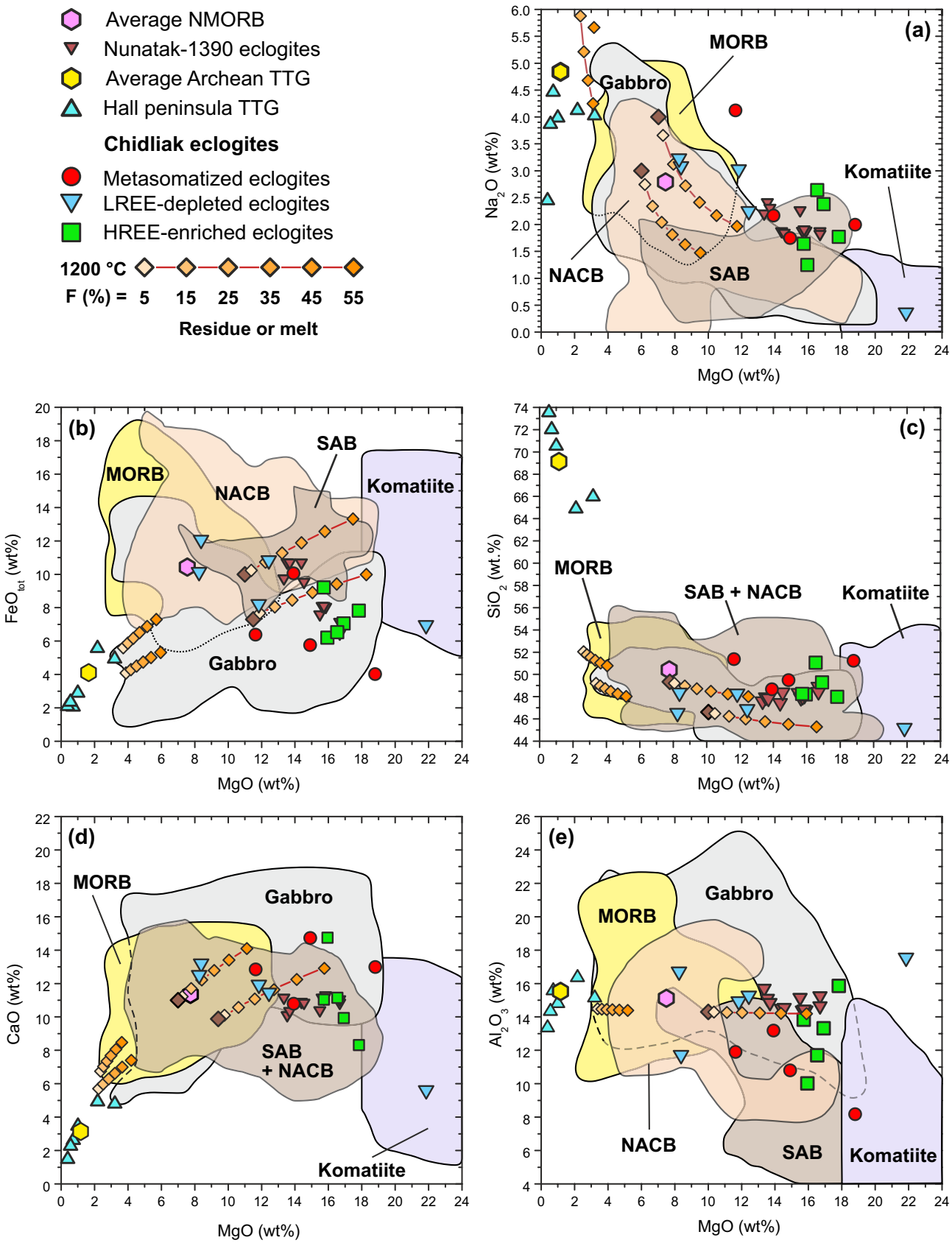
Average NMORB
Nunatak-1390 eclogites
Average Archean TTG
Hall peninsula TTG
Chidliak eclogites
Metasomatized eclogites
LREE-depleted eclogites
HREE-enriched eclogites
1200 °C
F (%) = 5 15 25 35 45 55
Residue or melt
(a)
MORB
Gabbro
Komatiite
NACB
SAB
Na2O (wt%)
MgO (wt%)
(b)
SAB
MORB
NACB
Komatiite
Gabbro
FeOtot (wt%)
MgO (wt%)
(c)
MORB
SAB + NACB
Komatiite
SiO2 (wt.%)
MgO (wt%)
(d)
MORB
Gabbro
SAB
+ NACB
Komatiite
CaO (wt%)
MgO (wt%)
(e)
Gabbro
MORB
NACB
SAB
Komatiite
Al2O3 (wt%)
MgO (wt%)

◂**Fig. 7** Major element variations in the reconstructed whole-rock compositions of the Chidliak eclogites (Online Resource 4) compared to potential crustal protoliths, eclogites and granites of the NAC and modeling data. The Nunatak-1390 eclogites ($n=11$) are after Tappe et al. (2011). The average Archean TTG composition is after Moyen and Martin (2012). The average NMORB composition is after Gale et al. (2013). Hall Peninsula TTG compositions ($n=6$) are after From et al. (2018). Superior Archean Basalt compositions for the partial melting modeling were chosen randomly. Eclogitic residue of a basaltic protolith and melt extraction has been modeled at $T=1200$ °C, $P=3.0$ GPa for an eclogitic composition with 50% of Cpx and 50% of Grt (batch melting). Partition coefficients between eclogitic minerals and melt (garnet–melt and clinopyroxene–melt) are after Green et al. (2000). The degree of partial melting ($F$) varies from 0.05 to 0.55 in 0.1 increments. The data for the gabbro (212 whole-rock samples) and MORB (4097 whole-rock samples and 17 737 samples of glasses) fields were downloaded from the PetDB Database (https://www.earthchem.org/petdb) and taken from single references (Online Resource 5). The gabbro field is based on the modern oceanic and ancient ophiolite gabbro dataset. The MORB field is based on compositions of whole-rock and NMORB glasses (normal MORB), EMORB (enriched MORB), DMORB (depleted MORB) and back-arc spreading center basalts (Online Resource 5). The data for the Superior Archean basalt (SAB) (98 whole-rock samples), NAC Archean basalt (NACB) (171 whole-rock samples) and komatiite (1825 whole-rock samples) fields were downloaded from the GEOROC Database (https://georoc.mpch-mainz.gwdg.de) (Online Resource 5). The SAB field comprises komatiitic basalts and picrites of Archean age from the Superior craton. The NACB field represents non-komatiitic basalts and picrites of Archean age from the NAC. The komatiite field includes only komatiite compositions of Archean age (Kerr and Arndt 2001)

presence of kyanite in sample CH-S9, which may be related to high whole-rock $Al_2O_3$ and high anorthite component in plagioclase (Jacob et al. 2009); (2) the high Sr content (2.4 ppm) in comparison with incompatible LREE (La, Ce, Pr, Eu 0.02–1.09 ppm, Online Resource 2) of garnet CH-D19-175, which cannot be related to kimberlite fluids because of low Nb (<0.5 ppm) in garnet and clinopyroxene (Aulbach and Jacob 2016); (3) a positive Eu anomaly (Eu/Eu* = 1.40) of CH-D19-175 REE pattern of garnet and RWR (Eu/Eu* = 1.38) (Fig. 4c). The degree of melting affected the gabbroic protoliths of the LREE-enriched eclogites remains uncertain as geochemical modeling is impossible in the absence of low-T, low-P experimental $K_D$ s relevant for TTG extraction (Moyen 2011). The other 15 eclogites do not show clear evidence of a gabbroic (plagioclase-rich) protolith; thus, most of the Chidliak eclogites reveal a genetic link to an Archean volcanic mafic protoliths. They may be more picritic than basaltic, as reflected in high MgO (12–22 wt% for 17 of 19 samples; Mg# of 67–85) (Fig. 7), and low Yb (< 2 ppm) contents at relatively high $TiO_2$ (0.5–2.4 wt%) (Aulbach and Viljoen 2015).

The inference of an insignificant role of gabbro and other plagioclase cumulates in the NAC subducting slabs contradicts the conclusion on the preferential subduction of lower parts of the plate during assembly of the Greenland NAC (Windley and Garde 2009). The West Greenland data on the tectonic history of NAC in the Archean suggest splitting of the subducting slabs into obducting and subducting parts. The upper crust (high-Mg basalts and boninites) may have been accreted and obducted, while the lower crust (anorthosites and gabbros) may have been subducted. Our petrological data on the Chidliak eclogites indicate that a significant proportion of the upper crustal basalts was also subducted.

The insights from trace elements are further augmented by comparison of reconstructed Chidliak major element bulk compositions with those of possible protoliths (Fig. 7). The protoliths could not have been MORB or komatiite, but may have been Archean greenstone belt basalt from the NAC or Superior craton, or gabbro. We invoked Archean basalts–picrites from both of these cratons for the analysis. NAC basalts show a geographical fit, but are older (ca. 3.8 or 3.1 Ga) (Dymek et al. 1988; Ordóñez-Calderón et al. 2011; Polat et al. 2002, 2008) than the 2.7–2.3 NAC eclogites (Sajeev et al. 2013; Tappe et al. 2011). Basalts from the Superior are closer in age (~2.7 Ga) (Barnes and Arndt 2019 and references therein) to the eclogites and there is a possibility of their subduction under NAC in the Paleoproterozoic during the cratons' merger. Archean basalts from the Superior craton and from NAC are richer in FeO than the Chidliak eclogites (Fig. 7b), but otherwise show a satisfactory match the eclogites. The latter also fall in the wide gabbro field (Fig. 7). An ideal major element compositional match between a protolith and a metamorphic product is not expected anyway, based on a complex history of partial melting, metasomatism and the open system metamorphism.

We tested the viability of residual origin for LREE-depleted Chdliak eclogites with major element modeling with a goal of reproducing local TTGs in the EHP (From 2017; From et al. 2018). For the modeling, we chose two arbitrary initial compositions within the wide basaltic protolith fields to demonstrate the trends of residues and extracted melts (Fig. 7). The plots for various major elements show that the extreme degree of partial melting, 55 vol%, increases the MgO by 10%, but this range is still inside the field of Superior and NAC Archean basalts or gabbros in all major elements ($Na_2O$, $SiO_2$, $Al_2O_3$ and MgO). Thus, both groups of the LREE-depleted (excluding two samples clearly related to gabbro protolith) and HREE-enriched Chidliak eclogites could have originated from the same protolith and differed only in the history of melt extraction.

## Signatures of mantle metasomatism in the Chidliak eclogites

Chidliak eclogites resided in the pervasively metasomatized peridotitic mantle (Kopylova et al. 2019) and may have been affected by several metasomatic events recorded in Chidliak peridotites, including the early (>1.4 Ga) silicate-carbonate

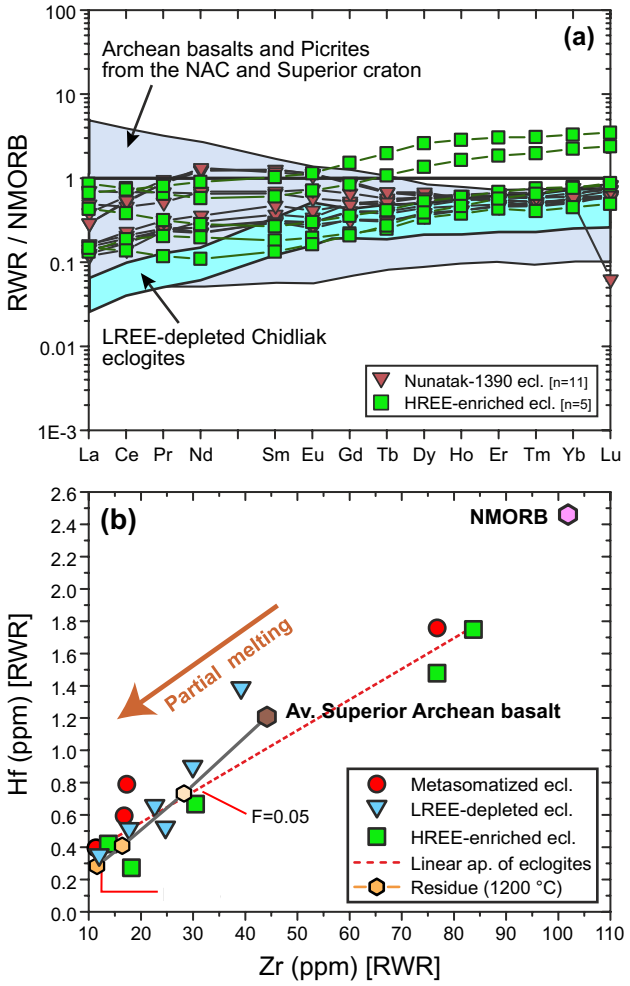


**Fig. 8** Reconstructed whole-rock (RWR) compositions of the Chidliak eclogites in comparison with Archean basalts and picrites from the Superior and North Atlantic cratons. **a** NMORB-normalized REE patterns of the RWR eclogite compositions. REE compositions of the Archean basalts and picrites from the Superior ($n=52$) and North Atlantic ($n=132$) cratons are given in Online Resource 5. **b** Zr vs. Hf for the Chidliak eclogites. The average Superior Archean basalt composition is based on 52 samples of Archean komatiitic basalt and Archean picrite (Online Resource 5). Parameters of the linear approximation of the Chidliak eclogites are PCC = 0.93 (Pearson correlation coefficient) and $R^2_{Adj}=0.85$ (adjusted coefficient of determination). Residue formation from batch melting of an eclogite with the average Archean basalt composition has been modeled at a temperature of 1200 °C at pressure of 3.0 GPa [partition coefficients after Green et al. (2000)] for eclogitic composition with 50% of Cpx and 50% of Grt. The degree of partial melting ($F$) varies from 0.05 to 0.55 in 0.1 increments

metasomatism and the more recent Ti metasomatism at $P=5.5$–$6.5$ GPa (180–215 km). The former is expressed in wehrlite formation, while the latter is seen in the increased Ti contents of peridotitic garnet and clinopyroxene and local deformation of peridotite due to hydrous weakening (Kopylova et al. 2019).

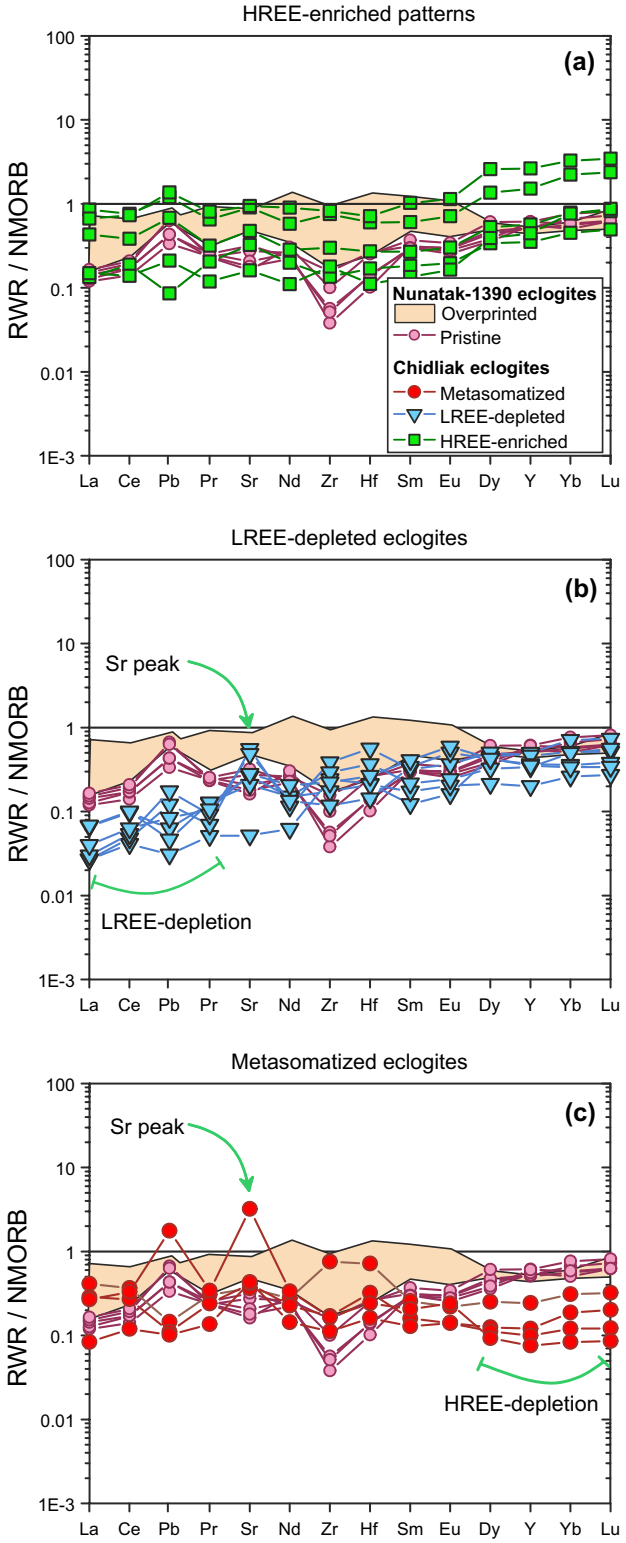


**Fig. 9** Comparison of NMORB-normalized trace element composition of the Chidliak (Table 1 of this study) and Nunatak-1390 (Tappe et al. 2011) eclogites (NAC). NMORB values are after Gale et al. (2013)

The silicate–carbonate metasomatism is reflected in several geochemical parameters of four eclogites classified as

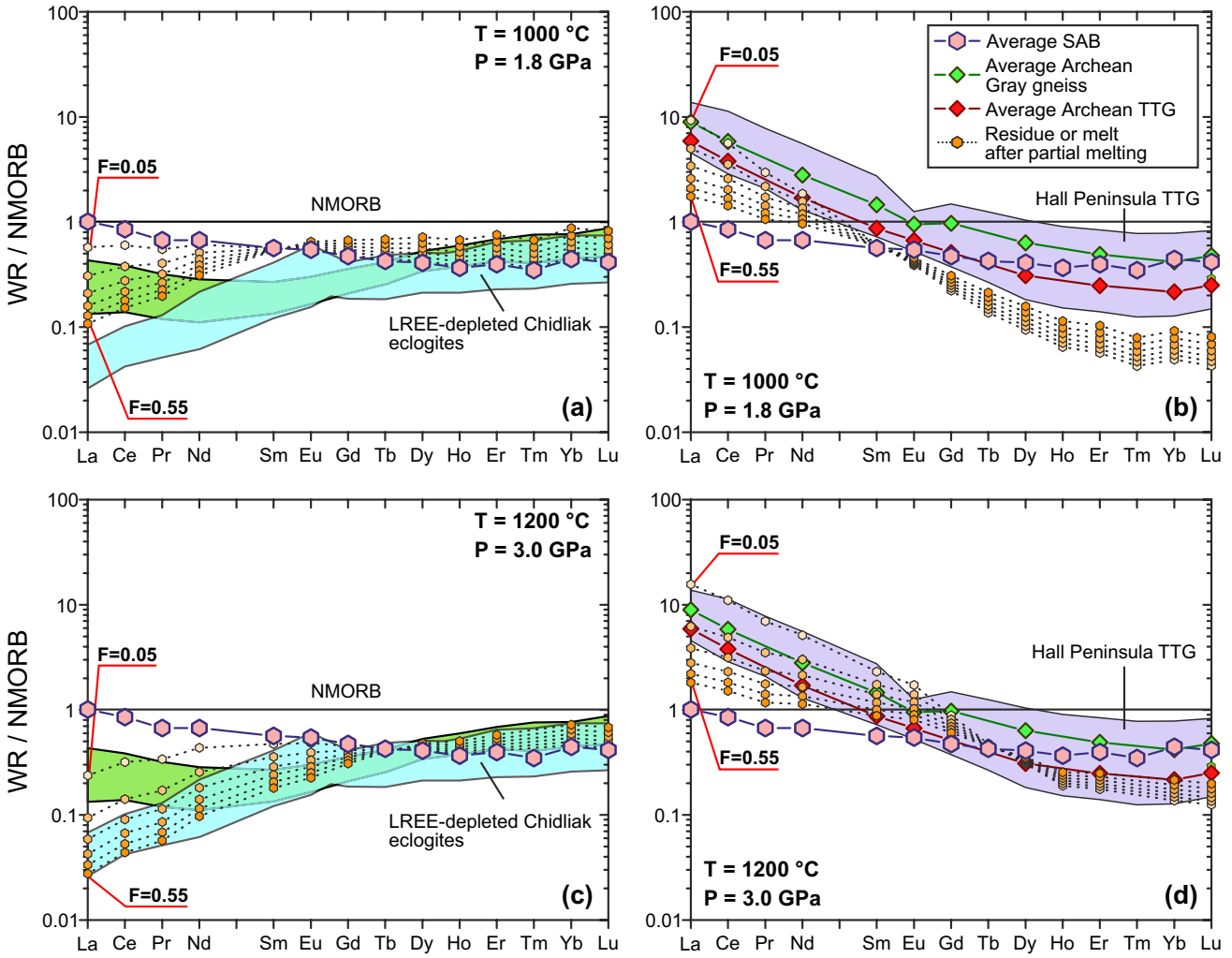


**Fig. 10** NMORB-normalized REE patterns of the average Superior Archean basalt (SAB) and modeled residues and partial melts. The difference in the NMORB-normalized REE patterns of the average NAC, SAB and worldwide Archean basalts is negligible (Online Resource 5). The average SAB has been chosen because of age complementarity reasons (please, see discussion in the text). Residues and melt formation have been modeled via batch melting at $T = 1000$ °C, $P = 1.8$ GPa (panels **a** and **b**) and $T = 1200$ °C, $P = 3.0$ GPa (panels **c** and **d**) for eclogitic composition with 50% of Cpx and 50% of Grt. Partition coefficients between eclogitic minerals and melt (garnet–melt and clinopyroxene–melt) for panels **a** and **b** are after Barth et al. (2002b) and for panels **c** and **d** are after Green et al. (2000). The degree of partial melting (F) varies from 0.05 to 0.55 in 0.1 increments. **a**, **c** Comparison of the residue compositions with the LREE-depleted (blue field) and HREE-enriched (green field) Chidliak eclogites. **b**, **d** Comparison of the partial melt compositions with the average Archean gray gneiss, TTG (Moyen and Martin 2012). The purple field includes the EHP TTG (Baffin Island) (From 2017) and Disko Bugt (West Greenland) TTG (Steenfelt et al. 2005). The compositions of EHP TTGs for the field were selected from a wider range of compositions reported by (From 2017), but deviating compositions with lower concentrations of REEs and positive Eu anomalies were not included

"metasomatized" based on reconstructed whole-rock LREE enrichment. The eclogites have NMORB-normalized Ce/Yb ratio of 1.0–4.0 at MgO of 11.6–18.8 wt% (Fig. 11a). The criteria of NMORB-normalized Ce/Yb > 1 at high $TiO_2 \geq 1$ wt% or high MgO ≥ 10 wt% were suggested by Aulbach and Jacob (2016) as indicators for metasomatism in eclogites if their protoliths are low-Yb basalts extracted from garnet-bearing deeper mantle. Secondly, NMORB-normalized Sr/Y of the RWR compositions (1.5–42.4) for metasomatized samples are significantly higher than the Sr/Y of HREE-enriched and LREE-depleted eclogites (0.1–1.3) (Fig. 11a). All of these signatures identify enrichment in LREE ($Ce_N/Yb_N$ 1.0–4.0) and Sr in comparison to the unmetasomatized Chidliak eclogites ($Ce_N/Yb_N$ 0.1–0.5) and average NMORB composition (Gale et al. 2013) (Fig. 11a; Online Resource 4). Moreover, garnet from one of the metasomatized eclogites (sample Q-B) exhibits a significantly modified REE pattern (Fig. 4d); while, clinopyroxene from another metasomatized sample (CH-D19-162) is extremely rich in Sr (624–640 ppm). High Sr (as well other LILE and

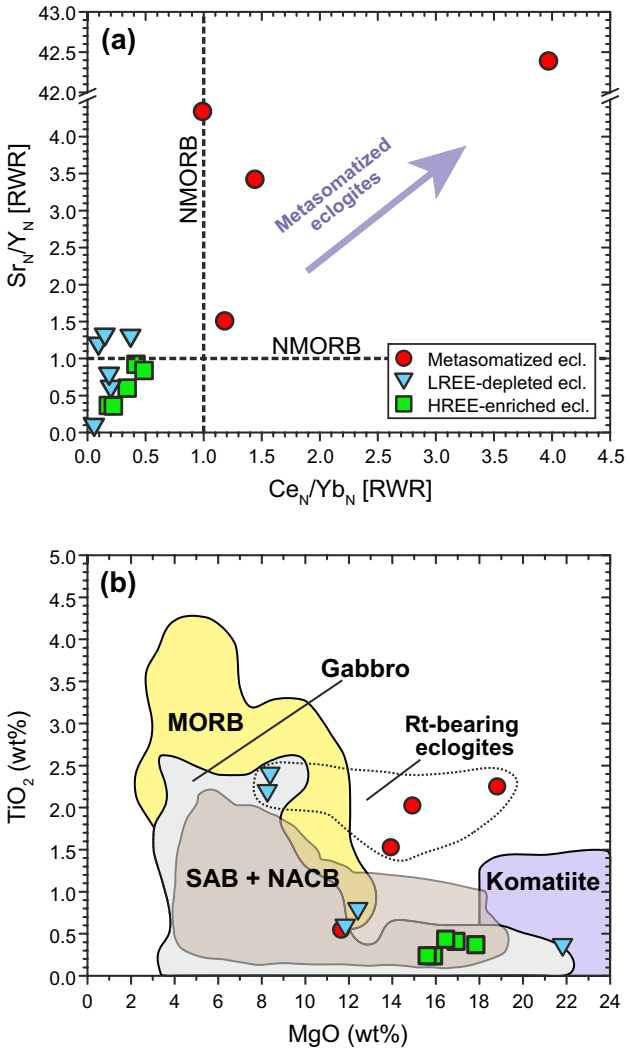


**Fig. 11** Reconstructed bulk rock compositions [RWR] of the Chidliak eclogites. **a** Trace-element ratios in the NMORB-normalized RWR compositions of the Chidliak eclogites in comparison with NMORB values from Gale et al. (2013). **b** MgO vs. $TiO_2$ for the Chidliak eclogites compared to potential crustal protoliths. Descriptions of the MORB, Gabbro, Superior Archean basalt (SAB), NAC Archean basalt (NACB) and Komatiite fields are provided in Fig. 7 caption

Th) is a sign of carbonate metasomatism (e.g., Deng et al. 2017; Yaxley et al. 1998) or could be inherited from a plagioclase-rich protolith. However, an association of Sr and LREE enrichment is best explained by metasomatism.

The more recent Ti metasomatism at Chidliak may have been reflected in very high RWR $TiO_2$ contents of rutile-bearing eclogites, exceeding 1.5 wt% and placing them outside fields for possible eclogite protoliths like gabbro or NAC and Superior Archean basalt (Fig. 11b). Additionally, the Ti metasomatism may manifest itself in the elevated temperatures of the eclogites controlled by the shifted Mg/Fe distribution between garnet and clinopyroxene. All three eclogites with super-adiabatic temperatures fall in the 5.5–6.5 GPa range of pressures if their temperatures are projected on the adiabat (Fig. 6b), i.e., fall in the depth range where Ti metasomatism is localized beneath Chidliak. These high-T eclogites may have experienced heating from an advecting asthenospheric metasomatic agent. If this fluid was saturated in $H_2O$ or in $H_2O$–$CO_2$, it would have caused partial melting of almost half of the Chidliak eclogites, as illustrated by the eclogite solidus temperatures at different fluid-saturated conditions (Fig. 6c). If so, partial eclogite melts would have contributed to this mobile hot fluid phase.

Another hallmark of mantle metasomatism observed in the Chidliak eclogites could be their high MgO and low FeO contents (Fig. 7). All groups of the Chidliak eclogites show FeO lower than in potential protoliths of NAC or Superior Archean basalts at a relatively high MgO contents (12–22 wt%) (Fig. 7b), which is typical for eclogite affected by carbonated ultramafic melt metasomatism (e.g., Aulbach et al. 2019). Higher RWR MgO contents may have resulted from recrystallization of clinopyroxene and garnet into metasomatic diopside-rich and pyrope-rich phases, the petrographically observable process reported multiple times for eclogites worldwide (Fig. 4 from De Stefano et al. 2009; Fig. 3 of Nikitina et al. 2014; Aulbach et al. 2007; Hills and Haggrety 1989; Ireland et al. 1994; Misra et al. 2004; Taylor and Anand 2004; Taylor and Neal 1989). The replacement of primary clinopyroxene and garnet with Mg-rich secondary clinopyroxene and garnet, respectively, along rims and in distinct patches is clearly seen in Chidliak, as demonstrated by the Mg-rich compositions of secondary clinopyroxene (Fig. 5). It is this process of metasomatic replacement by Mg-rich phases that may explain the difference in compositions between more sodic and less magnesian clinopyroxene diamond inclusions at Chidliak and more magnesian clinopyroxenes in eclogite xenoliths (Fig. 5). Minerals in diamonds shielded from metasomatism reflect the original nature of the eclogitic protolith; whereas, metasomatism adds MgO and leaches the jadeitic component from eclogitic clinopyroxenes.

## Comparison of NAC and Slave eclogites

Reconstructed major element compositions of the NAC (Chidliak and Nunatak-1390 localities, $n = 28$ samples) and Slave eclogites ($n = 287$, Online Resource 5) demonstrate a consistent difference. The NAC eclogites, on average, are more magnesian, less ferrous and less calcic. Only among Slave eclogites do we observe compositions matching MORBs based on the high Al and Fe. Statistical *t* tests (Table 3) determine that the average MgO and CaO contents of the NAC eclogites are distinct from the Slave eclogites with probability >99%, whilst the probability for FeO is 95%. The principal contribution in the identified contrast is the higher MgO and lower CaO of NAC garnet (distinct

**Table 3** Comparison of the statistical samples of the NAC and Slave eclogites (RWR, Cpx and Grt)

| Composition | RWR (50/50) | | Cpx | | Grt | |
|---|---|---|---|---|---|---|
| Craton | NAC | Slave | NAC | Slave | NAC | Slave |
| *N* | 28 | 287 | 28 | 309 | 30 | 403 |
| Av. MgO (wt%) | 14.58 | 11.88 | 12.97 | 11.51 | 15.75 | 12.43 |
| 1 σ | 2.88 | 3.67 | 1.94 | 3.13 | 4.22 | 4.50 |
| *t* test (calc.) | | 3.77 | | 2.43 | | 3.92 |
| Significance level | | | | | | |
| 1% | | 2.58 | | 2.58 | | 2.58 |
| 5% | | 1.96 | | 1.96 | | 1.96 |
| 10% | | 1.65 | | 1.65 | | 1.65 |
| Av. FeO (wt%) | 8.86 | 10.11 | 3.80 | 4.12 | 13.74 | 16.00 |
| 1 σ | 2.14 | 3.17 | 1.29 | 1.72 | 3.58 | 4.88 |
| *t* test (calc.) | | −2.05 | | −0.96 | | −2.49 |
| Significance level | | | | | | |
| 1% | | 2.58 | | 2.58 | | 2.58 |
| 5% | | 1.96 | | 1.96 | | 1.96 |
| 10% | | 1.65 | | 1.65 | | 1.65 |
| Av. CaO (wt%) | 11.16 | 12.23 | 16.92 | 16.33 | 6.05 | 8.07 |
| 1 σ | 1.39 | 1.56 | 1.96 | 3.15 | 3.95 | 3.22 |
| *t* test (calc.) | | −3.51 | | 0.97 | | −3.27 |
| Significance level | | | | | | |
| 1% | | 2.58 | | 2.58 | | 2.58 |
| 5% | | 1.96 | | 1.96 | | 1.96 |
| 10% | | 1.65 | | 1.65 | | 1.65 |

*NAC* North American Craton, *RWR* reconstructed whole-rock composition, *Grt* garnet, *Cpx* clinopyroxene, *Av* average, *N* number of samples

with probability >99%). This pattern is also manifest in the eclogite types as determined using the clinopyroxene mineral chemistry (Taylor and Neal 1989). Chidliak eclogites have a smaller proportion of C eclogites [5.6 vs 13.3% at N. Slave ($n = 158$) vs. 12.1% at C. Slave ($n = 124$)], counterbalanced by a larger proportion of B eclogites (66.7% vs 58.2 at N. Slave and 59.7 at C. Slave).

One of the possible explanations for the contrast is the stronger NAC metasomatism, whereby the elevated MgO of the NAC eclogites is controlled by the ultramafic nature of the metasomatic agent (Fig. 6c) and pervasive reaction with hydrous and silicate–carbonate fluids (Kopylova et al. 2019). The metasomatic control on composition of the Chidliak eclogitic clinopyroxene is observable in the contrast between clinopyroxene compositions shielded from and exposed to the metasomatism (Fig. 5). In contrast, Slave eclogites do not demonstrate a consistent difference between eclogitic inclusions in diamond and minerals in eclogitic xenoliths (Fig. 5b). In accordance with this, Slave peridotite xenoliths are less pervasively affected by metasomatism than Chidliak, as demonstrated by their textures and non-steady-state *P–T* arrays (Kopylova et al. 2019).

The contrasting bulk composition of mafic protoliths for the Slave and Chidliak eclogites may have contributed to their observed distinct major element chemistry (Table 3). It is possible that bulk compositions of basalts and picrites in greenstone belts on adjacent cratons differ significantly, as exemplified by the NAC and Superior cratons. Archean basalts–picrites from the NAC are not as compositionally wide as on the Superior craton, less magnesian, more aluminous and sodic (Fig. 7 as based on GEOROC Database: https://georoc.mpch-mainz.gwdg.de). Similar contrasts in major element compositions may have existed between basalts–picrites of the NAC and Slave cratons. The difference in age between the Archean NAC eclogites (Tappe et al. 2011) and Proterozoic Slave eclogites (Aulbach et al. 2009a, b; Heaman et al. 2006; Smart et al. 2014; Schmidberger et al. 2005) may have contributed to the contrast. Among the compared suites, only NAC eclogites may be representative of the uniquely Neoarchean melting process that extracted TTG, which imposed the distinct bulk composition to the residues. Further geochronological studies of NAC eclogites and comparative studies of Archean and Proterozoic eclogites worldwide would help to further assess the relative contributions of the three above factors.

## Position of eclogites in the mantle cross-section

The thermobarometry indicates that all Chidliak eclogites are equilibrated in the diamond *P–T* field (Fig. 6b) and, therefore, are potentially diamondiferous. This matches the preferential derivation of the Chidliak diamonds from eclogitic sources (Xia 2018), *P–T*s of the eclogitic Chidliak diamonds (Online Resource 6) similar to the high-temperature eclogites (Fig. 6b) and the Na-rich (≥0.09 wt%) character of all Chidliak eclogitic garnets, which is used (McCandless and Gurney 1989) as a hallmark of a deep origin and high diamond potential. The contradicting low K, diamond-barren affinity (McCandless and Gurney 1989) of Chidliak clinopyroxene (≤0.08 wt% $K_2O$) can be attributed to its preferential alteration.

NAC eclogites from Chidliak and Nunatak-1390 are distributed over >100 km depth in the diamond stability field of the upper mantle, from 120 to 250 km (Fig. 6; Online Resource 5). The distribution of peridotite and eclogite xenoliths are characterized by two traits: (1) the interval where peridotites are sampled most extensively (170–210 km) contains only a minor proportion of eclogites (3 out of 28 samples, 11%), but eclogites are present at depths shallower than peridotites; and (2) the interval is underlain by 30 km at the very base of the thermal lithosphere (220–250 km), where the predominant majority of xenoliths are eclogites (7 out of 8, 87%). These depths are in the asthenosphere as determined by surface wave inversions (Porritt et al. 2015). Interestingly, the deepest xenoliths from Chidliak are restricted only to eclogites. Overrepresentation of eclogite xenoliths (11% at Chidliak) with respect to eclogite abundance at depth (<4 vol%, Schulze 1989; Russell et al. 2001; McLean et al. 2007) common to all kimberlites (Gurney and Zweistra 1995), reaches the extreme in the 220–250 km depth interval.

The small sizes of continental blocks, their rich collisional history, multiple 100-km-long sutures and dipping mantle reflectors in the vicinity of EHP make it possible that the upper mantle of EHP is a collage of Archean and Proterozoic blocks. Below the northern Baffin Island, i.e., below the Meta Incognita microcontinent, some models suggest the underthrust Rae mantle beneath 150 km in the northern part and the underthrust superior mantle in the south (Fig. 10 of Snyder et al. 2017). Analysis of the deep mantle structure in the immediate vicinity of the Chidliak province was based on data from station FRB of the teleseismic survey of Snyder (2010) located in western Hall Peninsula. The joint analysis of receiver functions and SKS wave splitting identified several NE-dipping anisotropic layers at depths of 50–150 km (Snyder 2010). The authors hypothesized that the NAC mantle beneath the EHP might be underlain by subducted Proterozoic Narsajuaq Arc at 110–130 km, which, in turn, is underlain by the Superior craton [Fig. 4 of Snyder (2010)]. The eclogite-bearing depths do not match the identified NE-dipping anisotropic layers at 50–150 km (Snyder 2010), corroborating observations in the Slave mantle that eclogites are geophysically invisible and tend to be found in the weaker anisotropic horizons (Kopylova et al. 2016).

Eclogites occurring at 120–250 km beneath Chidliak may be attributed to subducted plates of different ages and orientations. It is possible that the Chidliak eclogites represent Archean subducted island arc crust. In this scenario, all NAC eclogites would have an Archean subduction origin, which may be similar to the age of Nunatak-1390 eclogites (2.70 ± 0.29 Ga; Tappe et al. 2011). The Archean origin of the Chidliak eclogites would broadly match the age of the NAC peridotitic mantle of 2.65 Ga in West Greenland (Wittig et al. 2010), the 2.4 Ga Re-Os ages ($T_{RD}$) of Chidliak peridotite xenoliths (Liu et al. 2017) and the crust of the EHP (2.98–2.72 Ga; From et al. 2018). The Chidliak eclogites would be autochthonous and synchronous with NAC mantle peridotites and NAC crustal TTG. Equally possible is the allochthonous origin of Chidliak eclogites, which may have been underthrust beneath the Archean NAC mantle as part of the Proterozoic subduction or the merged Archean Superior craton. Proterozoic subduction inserted eclogites beneath the Archean Slave peridotitic mantle (e.g., Heaman and Pearson 2010; Smart et al. 2014), where the eclogitic slab may have shielded the depleted lithosphere from the destructive asthenospheric metasomatism (Kopylova et al. 2016) and aided craton stabilization (Helmstaedt 2009). Perhaps, the presence of eclogites at the base of the NAC lithospheric mantle between 220 and 250 km (Fig. 6) played a protective role in the preservation of the cold, buoyant lithospheric mantle in the vicinity of the Davis Strait (Fig. 1). The Davis Strait is described as a bathymetric high comprising primarily of the incompletely destroyed continental lithosphere (Suckro et al. 2013) in between the new oceanic crust and mantle south in the Labrador Sea and north in the Baffin Bay (Heron et al. 2019). The lithospheric inheritance and the presence of eclogites at the lithosphere–asthenosphere boundary of the NAC may have been a potential controlling mechanism in the dynamics of the West Greenland rifting and the preservation of the continental Davis Strait (e.g., Peace et al. 2017, 2018).

The bimodal depth distribution of NAC eclogites (Fig. 6; Online Resource 6) also hints at a possibility of their dual origin. Shallow (above 170 km) Archean eclogites (including Nunatak-1390 eclogites) could be autochthonous and distinct from the deeper (>220 km) eclogites separated from the shallower samples by the peridotite-only mantle.

## Conclusions

1. The studied Chidliak eclogites are classified into three types based on their reconstructed whole-rock REE patterns, HREE-enriched, LREE-depleted and metasomatized.

2. The Chidliak eclogites are equilibrated in the diamond stability field at $T = 840–1410$ °C and $P = 4.1–7.4$ GPa.
3. The Chidliak eclogites exhibit clear and multiple signatures of crustal origin and may have originated from Archean basaltic and oceanic gabbro protoliths.
4. The LREE-depleted eclogites may have experienced 15–55% partial melting in the eclogite facies of metamorphism.
5. Eclogites of the NAC are statistically distinct from eclogites of the Slave craton in being more magnesian, less ferrous and less calcic. The contrast may relate to the stronger NAC metasomatism or to the different formation ages of the eclogites beneath the two cratons.

**Acknowledgements** The authors thank J. Pell, H. Grütter and Peregrine Diamonds Ltd. for access to samples. The study was funded by an NSERC Discovery Grant to M. Kopylova. Sonja Aulbach and an anonymous reviewer improved the quality of the manuscript by their constructive reviews.

## References

Arai H (2010) A function for the R programming language to recast garnet analyses into end-members: revision and porting of Muhling and Griffin's method. Comput Geosci 36:406–409. https://doi.org/10.1016/J.CAGEO.2009.05.007

Aulbach S, Jacob DE (2016) Major- and trace-elements in cratonic mantle eclogites and pyroxenites reveal heterogeneous sources and metamorphic processing of low-pressure protoliths. Lithos 262:586–605. https://doi.org/10.1016/J.LITHOS.2016.07.026

Aulbach S, Viljoen KS (2015) Eclogite xenoliths from the Lace kimberlite, Kaapvaal craton: from convecting mantle source to palaeo-ocean floor and back. Earth Planet Sci Lett 431:274–286. https://doi.org/10.1016/J.EPSL.2015.08.039

Aulbach S, Pearson NJ, O'Reilly SY, Doyle BJ (2007) Origins of xenolithic eclogites and pyroxenites from the central slave Craton, Canada. J Petrol 48:1843–1873. https://doi.org/10.1093/petrology/egm041

Aulbach S, Creaser RA, Pearson NJ, Simonetti SS, Heaman LM, Griffin WL, Stachel T (2009a) Sulfide and whole rock Re–Os systematics of eclogite and pyroxenite xenoliths from the Slave Craton, Canada. Earth Planet Sci Lett 283:48–58. https://doi.org/10.1016/j.epsl.2009.03.0s23

Aulbach S, Stachel T, Creaser RA, Heaman LM, Shirey SB, Muehlenbachs K, Harris JW (2009b) Sulphide survival and diamond genesis during formation and evolution of Archaean subcontinental lithosphere: a comparison between the Slave and Kaapvaal cratons. Lithos 112:747–757. https://doi.org/10.1016/j.lithos.2009.03.048

Aulbach S, Höfer HE, Gerdes A (2019) High-Mg and low-Mg mantle eclogites from Koidu (West African craton) linked by Neoproterozoic ultramafic melt metasomatism of subducted Archaean plateau-like oceanic crust. J Petrol 60:723–754. https://doi.org/10.1093/petrology/egz011

Aulbach S, Viljoen KS, Gerdes A (2020) Diamondiferous and barren eclogites and pyroxenites from the western Kaapvaal craton record subduction processes and mantle metasomatism, respectively. Lithos 368–369:105588. https://doi.org/10.1016/j.lithos.2020.105588

Barnes SJ, Arndt NT (2019) Distribution and geochemistry of komatiites and basalts through the Archean. Earth's oldest rocks, 2nd edn. Elsevier, The Amsterdam, pp 103–132. https://doi.org/10.1016/B978-0-444-63901-1.00006-X

Barth MG, Rudnick RL, Horn I et al (2001) Geochemistry of xenolithic eclogites from West Africa, part I: a link between low MgO eclogites and archean crust formation. Geochim Cosmochim Acta 65:1499–1527. https://doi.org/10.1016/S0016-7037(00)00626-8

Barth MG, Rudnick RL, Horn I et al (2002a) Geochemistry of xenolithic eclogites from West Africa, part 2: origins of the high MgO eclogites. Geochim Cosmochim Acta 66:4325–4345. https://doi.org/10.1016/S0016-7037(02)01004-9

Barth MG, Foley SF, Horn I (2002b) Partial melting in Archean subduction zones: constraints from experimentally determined trace element partition coefficients between eclogitic minerals and tonalitic melts under upper mantle conditions. Precambrian Res 113(3–4):323–340. https://doi.org/10.1016/S0301-9268(01)00216-9

Dasgupta R, Hirschmann MM, Withers AC (2004) Deep global cycling of carbon constrained by the solidus of anhydrous, carbonated eclogite under upper mantle conditions. Earth Planet Sci Lett 227:73–85. https://doi.org/10.1016/j.epsl.2004.08.004

Day HW (2012) A revised diamond–graphite transition curve. Am Mineral 97:52–62. https://doi.org/10.2138/am.2011.3763

Deng L, Liu Y, Zong K et al (2017) Trace element and Sr isotope records of multi-episode carbonatite metasomatism on the eastern margin of the North China Craton. Geochem Geophys Geosyst 18:220–237. https://doi.org/10.1002/2016GC006618

Desmons J, Smulikowski W (2007) A systematic nomenclature for metamorphic rocks: high P/T metamorphic rocks. In: Recomm. by IUGS Subcomm. Syst. Metamorph. Rocks. https://www.bgs.ac.uk/downloads/start.cfm?id=3188

Dyck B, Reno BL, Kokfelt TF (2015) The majorqaq belt: a record of neoarchaean orogenesis during final assembly of the North Atlantic Craton, southern West Greenland. Lithos 220–223:253–271. https://doi.org/10.1016/j.lithos.2015.01.024

Dymek RF, Brothers SC, Schiffries CM (1988) Petrogenesis of ultramafic metamorphic rocks from the 3800Ma Isua supracrustal belt, West Greenland. J Petrol 29:1353–1397. https://doi.org/10.1093/petrology/29.6.1353

Elazar O, Frost D, Navon O, Kessel R (2019) Melting of $H_2O$ and $CO_2$-bearing eclogite at 4–6 GPa and 900–1200 °C: implications for the generation of diamond-forming fluids. Geochim Cosmochim Acta 255:69–87. https://doi.org/10.1016/j.gca.2019.03.025

Foley SF, Buhre S, Jacob DE (2003) Evolution of the Archaean crust by delamination and shallow subduction. Nature 421:249–252. https://doi.org/10.1038/nature01319

From RE (2017) On the Archean geologic history of eastern Hall Peninsula, Baffin Island, Nunavut. University of Manitoba, Canada

From RE, Camacho A, Pearson DG, Luo Y (2018) U-Pb and Lu-Hf isotopes of the Archean orthogneiss complex on eastern Hall Peninsula, southern Baffin Island, Nunavut: Identification of exotic Paleo- to Mesoarchean crust beneath eastern Hall Peninsula. Precambrian Res 305:341–357. https://doi.org/10.1016/j.precamres.2017.12.024

Gale A, Dalton CA, Langmuir CH et al (2013) The mean composition of ocean ridge basalts. Geochem Geophys Geosyst 14:489–518. https://doi.org/10.1029/2012GC004334

Green TH, Blundy JD, Adam J, Yaxley GM (2000) SIMS determination of trace element partition coefficients between garnet, clinopyroxene and hydrous basaltic liquids at 2–7.5 GPa and 1080–1200 °C. Lithos 53:165–187. https://doi.org/10.1016/S0024-4937(00)00023-2

Gurney JJ, Zweistra P (1995) The interpretation of the major element compositions of mantle minerals in diamond exploration.

J Geochem Explor 53:293–309. https://doi.org/10.1016/0375-6742(94)00021-3
Hammouda T (2003) High-pressure melting of carbonated eclogite and experimental constraints on carbon recycling and storage in the mantle. Earth Planet Sci Lett 214:357–368. https://doi.org/10.1016/S0012-821X(03)00361-3
Hasterok D, Chapman DS (2011) Heat production and geotherms for the continental lithosphere. Earth Planet Sci Lett 307:59–70. https://doi.org/10.1016/J.EPSL.2011.04.034
Heaman LM, Pearson DG (2010) Nature and evolution of the Slave Province subcontinental lithospheric mantle. Can J Earth Sci 47:369–388. https://doi.org/10.1139/E09-046
Heaman LM, Creaser RA, Cookenboo HO, Chacko T (2006) Multistage modification of the northern Slave mantle lithosphere: evidence from zircon- and diamond-bearing eclogite xenoliths entrained in Jericho Kimberlite, Canada. J Petrol 47:821–858. https://doi.org/10.1093/petrology/egi097
Heaman LM, Pell J, Grütter HS, Creaser RA (2015) U-Pb geochronology and Sr/Nd isotope compositions of groundmass perovskite from the newly discovered Jurassic Chidliak kimberlite field, Baffin Island, Canada. Earth Planet Sci Lett 415:183–199. https://doi.org/10.1016/j.epsl.2014.12.056
Helmstaedt H (2009) Crust-mantle coupling revisited: the Archean Slave craton, NWT, Canada. Lithos 112:1055–1068. https://doi.org/10.1016/j.lithos.2009.04.046
Heron PJ, Peace AL, McCaffrey KJW et al (2019) Segmentation of rifts through structural inheritance: creation of the Davis Strait. Tectonics 38:2411–2430. https://doi.org/10.1029/2019tc005578
Hills DV, Haggerty SE (1989) Petrochemistry of eclogites from the Koidu Kimberlite complex, Sierra Leone. Contrib Mineral Petrol 103:397–422. https://doi.org/10.1007/BF01041749
Hunt L, Stachel T, Grutter H et al (2012) Small mantle fragments from the Renard kimberlites, Quebec: powerful recorders of mantle lithosphere formation and modification beneath the Eastern Superior Craton. J Petrol 53:1597–1635. https://doi.org/10.1093/petrology/egs027
Ireland TR, Rudnick RL, Spetsius Z (1994) Trace elements in diamond inclusions from eclogites reveal link to Archean granites. Earth Planet Sci Lett 128:199–213. https://doi.org/10.1016/0012-821X(94)90145-7
Jacob DE (2004) Nature and origin of eclogite xenoliths from kimberlites. Lithos 77:295–316. https://doi.org/10.1016/J.LITHOS.2004.03.038
Jacob DE, Viljoen KS, Grassineau NV (2009) Eclogite xenoliths from Kimberley, South Africa—a case study of mantle metasomatism in eclogites. Lithos 112:1002–1013. https://doi.org/10.1016/J.LITHOS.2009.03.034
Katsura T, Yoneda A, Yamazaki D et al (2010) Adiabatic temperature profile in the mantle. Phys Earth Planet Inter 183:212–218. https://doi.org/10.1016/j.pepi.2010.07.001
Kerr AC, Arndt NT (2001) A note on the IUGS reclassification of the high-Mg and picritic volcanic rocks. J Petrol 42:2169–2171. https://doi.org/10.1093/petrology/42.11.2169
Kessel R, Ulmer P, Pettke T et al (2005) The water-basalt system at 4 to 6 GPa: phase relations and second critical endpoint in a K-free eclogite at 700 to 1400 °C. Earth Planet Sci Lett 237:873–892. https://doi.org/10.1016/j.epsl.2005.06.018
Kopylova MG, Beausoleil Y, Goncharov A et al (2016) Spatial distribution of eclogite in the Slave cratonic mantle: the role of subduction. Tectonophysics 672–673:87–103. https://doi.org/10.1016/j.tecto.2016.01.034
Kopylova MG, Tso E, Ma F, Liu J, Pearson DG (2019) The metasomatized mantle beneath the North Atlantic Craton: insight from peridotite xenoliths of the Chidliak kimberlite province (NE Canada). J Petrol 60:1991–2024. https://doi.org/10.1093/petrology/egz061
Leahy K, Taylor WR (1997) The influence of the Glennie domain deep structure on the diamondsin Saskatchewan kimberlites. Geol Geofizika 38:451–460
Liu J, Pearson DG, Harris GA, et al (2017) Age and evolution of the lithospheric mantle beneath southern Baffin Island, Nunavut, Canada. In: International Kimberlite Conference: Extended Abstracts, vol. 11, pp 11IKC–4584
Mather KA, Pearson DG, McKenzie D et al (2011) Constraints on the depth and thermal history of cratonic lithosphere from peridotite xenoliths, xenocrysts and seismology. Lithos 125:729–742. https://doi.org/10.1016/j.lithos.2011.04.003
McCandless TE, Gurney JJ (1989) Sodium in garnet and potassium in clinopyroxene: criteria for classifying mantle eclogites. In: Ross J, Jaques AL, Ferguson J, et al. (Eds) Kimberlites and Related Rocks, vol. 2, pp 827–832
McDonough WF, Sun S-s (1995) The composition of the earth. Chem Geol 120:223–253. https://doi.org/10.1016/0009-2541(94)00140-4
McLean H, Banas A, Creighton S et al (2007) Garnet xenocrysts from the Diavik mine, NWT, Canada: composition, color, and paragenesis. Can Mineral 45:1131–1145. https://doi.org/10.2113/gscanmin.45.5.1131
Misra KC, Anand M, Taylor LA, Sobolev NA (2004) Multi-stage metasomatism of diamondiferous eclogite xenoliths from the Udachnaya kimberlite pipe, Yakutia, Siberia. Contrib Mineral Petrol 146:696–714. https://doi.org/10.1007/s00410-003-0529-z
Morimoto N (1988) Nomenclature of pyroxenes. Mineral Petrol 39:55–76. https://doi.org/10.1007/BF01226262
Moyen JF (2011) The composite Archaean grey gneisses: petrological significance, and evidence for a non-unique tectonic setting for Archaean crustal growth. Lithos 123:21–36. https://doi.org/10.1016/j.lithos.2010.09.015
Moyen JF, Martin H (2012) Forty years of TTG research. Lithos 148:312–336. https://doi.org/10.1016/j.lithos.2012.06.010
Nakamura D (2009) A new formulation of garnet-clinopyroxene geothermometer based on accumulation and statistical analysis of a large experimental data set. J Metamorph Geol 27:495–508. https://doi.org/10.1111/j.1525-1314.2009.00828.x
Nickel KG, Green DH (1985) Empirical geothermobarometry for garnet peridotites and implications for the nature of the lithosphere, kimberlites and diamonds. Earth Planet Sci Lett 73:158–170. https://doi.org/10.1016/0012-821X(85)90043-3
Nikitina LP, Korolev NM, Zinchenko VN, Felix JT (2014) Eclogites from the upper mantle beneath the Kasai Craton (Western Africa): petrography, whole-rock geochemistry and U-Pb zircon age. Precambrian Res 249:13–32. https://doi.org/10.1016/j.precamres.2014.04.014
Nimis P, Grütter H (2010) Internally consistent geothermometers for garnet peridotites and pyroxenites. Contrib Mineral Petrol 159:411–427. https://doi.org/10.1007/s00410-009-0455-9
Ordóñez-Calderón JC, Polat A, Fryer BJ, Gagnon JE (2011) Field and geochemical characteristics of Mesoarchean to Neoarchean volcanic rocks in the Storø greenstone belt, SW Greenland: evidence for accretion of intra-oceanic volcanic arcs. Precambrian Res 184:24–42. https://doi.org/10.1016/j.precamres.2010.10.003
Paton C, Hellstrom J, Paul B et al (2011) Iolite: freeware for the visualisation and processing of mass spectrometric data. J Anal At Spectrom 26:2508–2518. https://doi.org/10.1039/c1ja10172b
Peace AL, Foulger GR, Schiffer C, McCaffrey KJW (2017) Evolution of Labrador Sea-Baffin Bay: plate or plume processes. Geosci Canada. 44:91–102. https://doi.org/10.12789/geocanj.2017.44.120
Peace A, McCaffrey K, Imber J et al (2018) The role of pre-existing structures during rifting, continental breakup and transform system development, offshore West Greenland. Basin Res 30:373–394. https://doi.org/10.1111/bre.12257

Pearson DG, Wittig N (2014) The formation and evolution of cratonic mantle lithosphere-evidence from mantle xenoliths. In: Holland HD, Turekian KK (eds) Treatise on geochemistry, 2nd edn. Elsevier Ltd, Amsterdam, pp 255–292

Pell J, Clements B, Grütter H, et al (2013) Following kimberlite indicator minerals to source in the Chidliak kimberlite province, Nunavut. In: Paulen RC, McClenaghan MB (Eds) Geological Survey of Canada. pp 21–26

Polat A, Hofmann AW, Rosing MT (2002) Boninite-like volcanic rocks in the 3.7–3.8 Ga Isua greenstone belt, West Greenland: geochemical evidence for intra-oceanic subduction zone processes in the early Earth. Chem Geol 184:231–254. https://doi.org/10.1016/S0009-2541(01)00363-1

Polat A, Frei R, Appel PWU, Dilek Y, Fryer B, Ordóñez-Calderón JC, Yang Z (2008) The origin and compositions of Mesoarchean oceanic crust: evidence from the 3075 Ma Ivisaartoq greenstone belt, SW Greenland. Lithos 100:293–321. https://doi.org/10.1016/j.lithos.2007.06.021

Poli S (2015) Carbon mobilized at shallow depths in subduction zones by carbonatitic liquids. Nat Geosci 8:633–636. https://doi.org/10.1038/ngeo2464

Porritt RW, Miller MS, Darbyshire FA (2015) Lithospheric architecture beneath Hudson Bay. Geochem Geophys Geosyst 16:2262–2275. https://doi.org/10.1002/2015GC005845

Pouchou JL, Pichoir F (1985) "PAP" φ(ρZ) procedure for improved quantitative microanalysis. In: Armstrong JL (ed) Microbeam analysis. San Francisco Press Inc., San Francisco, pp 104–106

Russell JK, Dipple GM, Kopylova MG (2001) Heat production and heat flow in the mantle lithosphere, Slave craton, Canada. Phys Earth Planet Inter 123:27–44. https://doi.org/10.1016/S0031-9201(00)00201-6

Sajeev K, Windley BF, Hegner E, Komiya T (2013) High-temperature, high-pressure granulites (retrogressed eclogites) in the central region of the Lewisian, NW Scotland: crustal-scale subduction in the Neoarchaean. Gondwana Res 23:526–538. https://doi.org/10.1016/j.gr.2012.05.002

Schmidberger SS, Heaman LM, Simonetti A et al (2005) Formation of Paleoproterozoic eclogitic mantle, Slave Province (Canada): Insights from in-situ Hf and U-Pb isotopic analyses of mantle zircons. Earth Planet Sci Lett 240:621–633. https://doi.org/10.1016/j.epsl.2005.09.057

Schulze DJ (1989) Constraints on the abundance of eclogite in the upper mantle. J Geophys Res Solid Earth 94:4205–4212. https://doi.org/10.1029/JB094iB04p04205

Scott DJ, Stern RA, St-Onge MR, McMullen SM (2002) U-Pb geochronology of detrital zircons in metasedimentary rocks from southern Baffin Island: implications for the Paleoproterozoic tectonic evolution of Northeastern Laurentia. Can J Earth Sci 39:611–623. https://doi.org/10.1139/e01-093

Smart KA, Chacko T, Simonetti A et al (2014) A record of Paleoproterozoic subduction preserved in the northern Slave cratonic mantle: Sr-Pb-O isotope and trace-element investigations of eclogite xenoliths from the Jericho and Muskox kimberlites. J Petrol 55:549–583. https://doi.org/10.1093/petrology/egt077

Snyder DB (2010) Mantle lithosphere structure beneath southeast Baffin Island, Nunavut from teleseismic studies. Geolog Surv Canada Curr Res 2010–8:1–6

Snyder GA, Taylor LA, Crozaz G et al (1997) The origins of Yakutian eclogite xenoliths. J Petrol 38:85–113. https://doi.org/10.1093/petroj/38.1.85

Snyder DB, Humphreys E, Pearson DG (2017) Construction and destruction of some North American cratons. Tectonophysics 694:464–485. https://doi.org/10.1016/j.tecto.2016.11.032

De Stefano A, Kopylova MG, Cartigny P, Afanasiev V (2009) Diamonds and eclogites of the Jericho kimberlite (Northern Canada). Contrib Mineral Petrol 158:295–315. https://doi.org/10.1007/s00410-009-0384-7

Steenfelt A, Garde AA, Moyen JF (2005) Mantle wedge involvement in the petrogenesis of Archaean grey gneisses in West Greenland. Lithos 79:207–228. https://doi.org/10.1016/j.lithos.2004.04.054

St-Onge MR, Scott DJ, Wodicka N (2002) Review of crustal architecture and evolution in the Ungava Peninsula—Baffin Island area: connection to the Lithoprobe ECSOOT transect. Can J Earth Sci 39:589–610. https://doi.org/10.1139/e02-022

Sturm R (2002) PX-NOM—an interactive spreadsheet program for the computation of pyroxene analyses derived from the electron microprobe. Comput Geosci 28:473–483. https://doi.org/10.1016/S0098-3004(01)00083-8

Suckro SK, Gohl K, Funck T et al (2013) The Davis Strait crust—a transform margin between two oceanic basins. Geophys J Int 193:78–97. https://doi.org/10.1093/gji/ggs126

Tappe S, Smart KA, Pearson DG et al (2011) Craton formation in Late Archean subduction zones revealed by first Greenland eclogites. Geology 39:1103–1106. https://doi.org/10.1130/G32348.1

Taylor WR (1998) An experimental test of some geothermometer and geobarometer formulations for upper mantle peridotites with application to the thermobarometry of fertile lherzolite and garnet websterite. Neues Jahrb für Mineral Abhandlungen 172:381–408. https://doi.org/10.1127/NJMA/172/1998/381

Taylor LA, Anand M (2004) Diamonds: time capsules from the Siberian Mantle. Geochemistry 64:1–74. https://doi.org/10.1016/j.chemer.2003.11.006

Taylor LA, Neal CR (1989) Eclogites with oceanic crustal and mantle signatures from the Bellsbank kimberlite, South Africa, Part I: mineralogy, petrography, and whole rock chemistry. J Geol 97:551–567. https://doi.org/10.1086/629334

Taylor WR, Jaques AL, Ridd M (1990) Nitrogen-defect aggregation characteristics of some Australasian diamonds; time-temperature constraints on the source regions of pipe and alluvial diamonds. Am Mineral 75:1290–1310

Thompson DA, Bastow ID, Helffrich G et al (2010) Precambrian crustal evolution: seismic constraints from the Canadian Shield. Earth Planet Sci Lett 297:655–666. https://doi.org/10.1016/j.epsl.2010.07.021

Thomson AR, Walter MJ, Kohn SC, Brooker RA (2016) Slab melting as a barrier to deep carbon subduction. Nature 529:76–79. https://doi.org/10.1038/nature16174

Windley BF, Garde AA (2009) Arc-generated blocks with crustal sections in the North Atlantic craton of West Greenland: crustal growth in the Archean with modern analogues. Earth Sci Rev 93:1–30. https://doi.org/10.1016/j.earscirev.2008.12.001

Wittig N, Webb M, Pearson DG et al (2010) Formation of the North Atlantic Craton: timing and mechanisms constrained from Re-Os isotope and PGE data of peridotite xenoliths from S.W. Greenland Chem Geol 276:166–187. https://doi.org/10.1016/j.chemgeo.2010.06.002

Xia X (2018) Mineral inclusions in diamonds from Chidliak (Nunavut, Canada): constraining the diamond substrates. MSc Thesis, University of Alberta

Yasuda A, Fujii T, Kurita K (1994) Melting phase relations of an anhydrous mid-ocean ridge basalt from 3 to 20 GPa: implications for the behavior of subducted oceanic crust in the mantle. J Geophys Res 99:9401–9414. https://doi.org/10.1029/93JB03205

Yaxley GM, Green DH, Kamenetsky V (1998) Carbonatite Metasomatism in the Southeastern Australian Lithosphere. J Petrol 39:1917–1930. https://doi.org/10.1093/petroj/39.11-12.1917